

# SUPRAMOLECULARLY ORGANIZED LUMINESCENT DYE MOLECULES IN THE CHANNELS OF ZEOLITE L\*

Gion Calzaferri<sup>a</sup>, Huub Maas, Marc Pauchard, Michel Pfenniger,  
Silke Megelski, André Devaux

Department of Chemistry and Biochemistry,  
University of Bern, Freiestrasse 3, CH-3000 Bern 9, Switzerland

**keywords:** energy migration, energy transfer, supramolecular, zeolite L, spectral overlap, light harvesting.

## CONTENTS

- I. Introduction
- II. The System
  - A. Geometrical Constraints
  - B. Inner and Outer Surface of the Zeolite Nanocrystals
  - C. The Dyes
  - D. Three-dye Antenna
  - E. The Stopcock Principle
- III. Transfer of Electronic Excitation Energy
  - A. Radiationless Energy Transfer
  - B. Förster Energy Transfer in Dye Loaded Zeolite L
  - C. Spectral Overlap
- IV. Elegant Experiments for Visual Proof of Energy Transfer and Migration
  - A. Energy Transfer
  - B. Intrazeolite Diffusion Monitored by Energy Transfer
  - C. Energy Migration
- V. Conclusions
- References

\* Dedicated to professor Ernst Schumacher on the occasion of his 75th birthday.

<sup>a</sup> email: Gion.Calzaferri@iac.unibe.ch

## I. INTRODUCTION

An important aim of photochemistry is to discover or to design structurally organized and functionally integrated artificial systems which are capable of elaborating the energy and information input of photons to perform useful functions such as transformation and storage of solar energy, processing and storage of information, sensing the microscopic environment on a molecular level. The complexity and beauty of natural systems have encouraged chemists to study the structure and properties of organized media like molecular crystals, liquid crystals and related regular arrangements and to mimic some of their functions. Microporous structures containing atoms, clusters, molecules or complexes provide a source of new materials with exciting properties [1-6]. For this purpose, zeolites are especially appealing crystalline inorganic microporous materials. Some of them occur in nature as a component of the soil. Natural and synthetic zeolites possess a large variety of well-defined internal structures such as uniform cages, cavities or channels [7, 8, 9, 10]. A useful feature of zeolites is their ability to host molecular guests within the intravoid space. Chromophore loaded zeolites have been investigated for different purposes such as interfacial electron transfer, microlasers, second harmonic generation, frequency doubling and optical bistabilities giving rise to persistent spectral hole burning [11-21]. The role of the zeolite framework is to act as a host for realizing the desired geometrical properties and for stabilizing the incorporated molecules. Incorporation of chromophores into the cavities of zeolites can be achieved in different ways, depending on the used substances and on the desired properties: from the gas phase [22-24], by ion exchange if cations are involved [3, 25-28] by crystallization inclusion [29] or by performing an *in situ* synthesis inside the zeolite cages [30, 31].

Plants are masters of efficiently transforming sunlight into chemical energy. In this process, every plant leaf acts as a photonic antenna system, in which photonic energy is absorbed in the form of sunlight and transported by chlorophyll molecules for the purpose of energy transformation. In natural photosynthesis, light is absorbed by an antenna system of a few hundred chlorophyll molecules arranged in a protein environment. The antenna system allows a fast energy transfer from an electronically excited molecule to unexcited neighbor molecules in a way that the excitation energy reaches the reaction center with high probability. Trapping occurs there. It has been reported that the anisotropic arrangement of chlorophyll molecules is important for efficient energy migration [32, 33]. In natural antenna systems the formation of aggregates is prevented by fencing the chlorophyll molecules in polypeptide cages [34]. A similar approach is possible by enclosing dyes inside a microporous material and by choosing conditions such that the volume of the cages and channels is able to uptake only monomers but not aggregates.

An artificial photonic antenna system is an organized multi-component arrangement in which several chromophoric molecular species absorb the incident light and transport the excitation energy (not charges) to a common acceptor component. Imaginative attempts to build an artificial antenna different from ours have been presented in the literature [35]. Multinuclear luminescent metal complexes [36-38], multichromophore cyclodextrins [39], Langmuir Blodgett films [40-43], dyes in polymer matrices [44-46] and dendrimers [47] have been investigated. Some sensitization processes in silver halide photographic materials [48] and also the spectral sensitization of polycrystalline titanium dioxide films bear in some cases aspects of artificial antenna systems [49-51]. However, to our knowledge the system reported in [3, 22, 52, 53] is the first artificial antenna which works well enough to deserve this name. It is of a bi-directional type, based on zeolite L as a host material, and able to collect and transport excitation over relatively large distances. The light transport is made possible by

specifically organized dye molecules which mimic the natural function of chlorophyll. The zeolite L crystals consist of a continuous one-dimensional tube system. We have filled each individual tube with successive chains of different joint but non-interacting dye molecules. Light shining on the cylinder is first absorbed and the energy is then transported by the dye molecules inside the tubes to the cylinder ends.

A schematic view of the artificial antenna is illustrated in Fig. 1. The monomeric dye molecules are represented by rectangles. The dye molecule which has been excited by absorbing an incident photon transfers its electronic excitation to another one. After a series of such steps the electronic excitation reaches a trap which we have pictured as shaded rectangles. The energy migration is in competition with spontaneous emission, radiationless decay and photochemically induced degradation. Very fast energy migration is therefore crucial if a trap should be reached before other processes can take place. These conditions impose not only spectroscopic but also decisive geometrical constraints on the system.

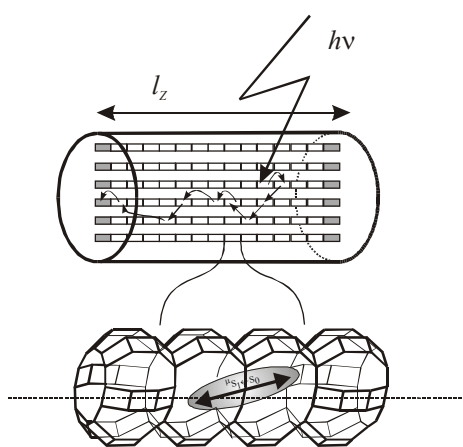


**Figure 1.** Representation of a cylindrical nanocrystal consisting of organized dye molecules acting as donors (empty rectangles) and an acceptor acting as trap at the front and the back of each channel (shaded rectangles). The enlargement shows a detail of the zeolite L channel with a dye molecule and its electronic transition moment. The orientation of this electronic transition moment with respect to the long axis depends on the length and shape of the molecules [54].

In the present article we describe the design and important properties of supramolecularly organized dye molecules in the channels of hexagonal nanocrystals. We focus on zeolite L as a host. The principles, however, hold for other materials as well. As an example we mention ZSM-12 for which some preliminary results have been reported [55]. We have developed different methods for preparing well defined dye-zeolite materials, working for cationic dyes, neutral dyes and combinations of them [3, 22, 25, 52]. The formula and trivial names of the many dyes which so far have been inserted in zeolite L are reported in Section II-C. The properties of natural and commercially available zeolites can be influenced dramatically by impurities formed by transition metals, chloride, aluminiumoxide and other. This fact it is not always sufficiently taken care of. In this article we only report results on chemically pure zeolites the synthesis of which is described in [53].

## II. THE SYSTEM

Favorable conditions for realizing a device as illustrated in Fig. 1 are a high concentration of monomeric dye molecules with high luminescence quantum yield, ideal geometrical arrangement of the chromophores and an optimal size of the device. Dyes at high concentration have the tendency to form aggregates which in general show very fast radiationless decay [56], [57]. The formation of aggregates can be prevented by fencing dyes inside a microporous material and by choosing conditions such that the volume of the cages and channels is only able to uptake monomers but not aggregates. Linear channels running through microcrystals allow the formation of highly anisotropic dye assemblies. Examples of zeolites bearing such channels, large enough to uptake organic dye molecules are reported in Table 1. Our investigations have been concentrated on zeolite L as a host. The reason for this is that neutral dyes as well as cationic dyes can be inserted into the channels of zeolite L and that synthesis procedures for controlling the morphology of zeolite L crystals in the size regime from 30 nm to about 3000 nm are available [53, 58-60]. Many results obtained on zeolite L are valid for other nanoporous materials as well. In Fig. 2 we show a scanning electron microscopy picture of a zeolite L material with nice morphology. The hexagonal shape of the crystals can easily be recognized. For simplicity we often describe them as crystals of cylinder morphology.

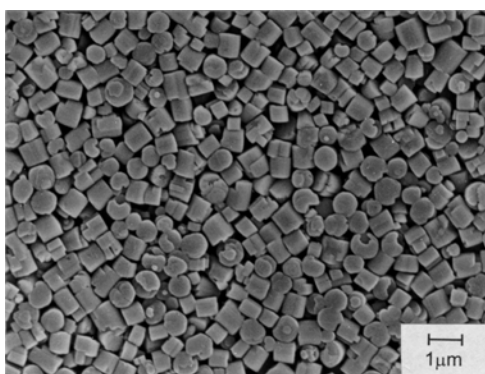


**Figure 2.** Scanning electron microscopy picture of a zeolite L sample [25].

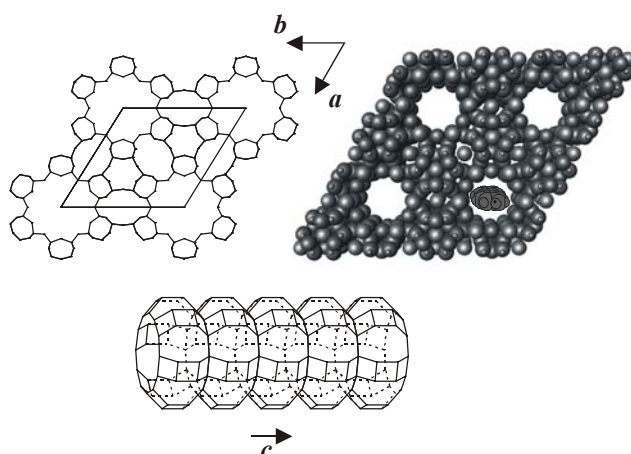


**Figure 3.** Framework of zeolite L. *Upper:* top view, perpendicular to the  $c$ -axis, displayed as stick- (left) and as Van der Waals- (right) representation with a dye molecule entering the zeolite channel. *Lower:* Side view of a channel along the  $c$ -axis, without bridging oxygen atoms.

A space filling top view and a side view of the zeolite L framework is illustrated in Fig. 3. The primitive vector  $c$  corresponds to the channel axis while the primitive vectors  $a$  and  $b$  are perpendicular to it, enclosing an angle of  $60^\circ$ .

We distinguish between three types of dye molecules. (i) *Molecules small enough to fit into a single unit cell.* Examples we have investigated so far are biphenyl, hydroxy-TEMPO, fluorenone and methylviologen ( $MV^{2+}$ ). Structural details of the latter are known based on vibrational spectroscopy, Rietveld refinement of X-ray data and molecular modeling. We found that the  $MV^{2+}$  lies along the channel wall, and that the angle between the main  $MV^{2+}$  axis and the  $c$ -axis of the zeolite is  $27^\circ$  [25]. (ii) *Molecules with a size which makes it hard to guess if they align along the  $c$ -axis or if they find a way to fit into a single unit cell.* Oxonine, Pyronine and Thionine are molecules of this type, as we will see later. (iii) *Molecules which are so large that they have no other choice but to align along the  $c$ -axis.* Many examples fit into this category. The POPOP illustrated in Fig. 4 is one of them. It is important to know if molecules can occupy at least part of the same unit cell, so that they can interact via their  $\pi$ -system or if they can "only touch each other" so that their electronic coupling is negligible.

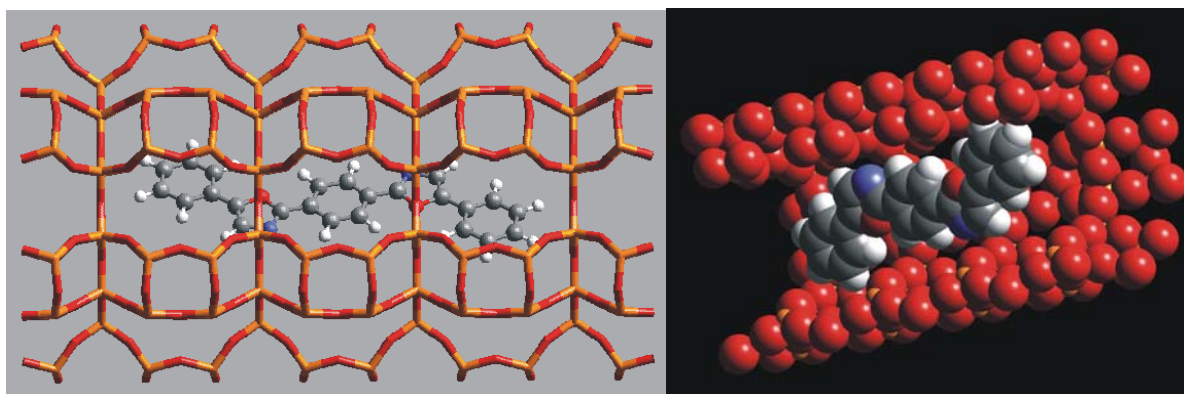


**Figure 4.** Illustration of the length and space filling POPOP in zeolite L.

While for molecules of type (i) not only translational but also large amplitude modes can be activated, the latter are severely or even fully restricted for molecules of type (ii) and (iii). This has consequences on their stability and also their luminescence quantum yield which in general increases. An example which we have investigated is the very light sensitive DPH which is dramatically stabilized when inserted into zeolite L, because there is not sufficient space available for trans to cis isomerisation [22]. In other cases a dramatic increase of stability is observed because reactive molecules which are too large or anions such as hypochlorite have no access because they can not enter the negatively charged channels [3, 61]. It is not surprising that the fluorescence quantum yield of cationic dyes is not or only positively affected by the zeolite L framework. More interestingly, the fluorescence quantum yield of neutral dyes also seems to be positively influenced by the zeolite L framework despite of the very large ionic strength inside the channels. Only one case of an anionic organic dye in the anionic zeolite L framework has been reported so far, namely the resorufin. This is also the only case where severe luminescence quenching has been observed [23]. Most results reported here refer to dye loaded zeolite L material which contains several water molecules per unit cell, see [22]. If the water molecules are completely removed from the main channel, the spectroscopic properties may change.

**TABLE 1** Lattice constants  $a$ ,  $b$ , and  $c$  and free opening diameters  $\emptyset$  of hexagonal molecular sieves with linear channels (in nm) [8]

	$a = b$	$c$	$\emptyset$
Mazzite	1.84	0.76	0.74
AlPO <sub>4</sub> -5	1.34	0.84	0.73
Zeolite L	1.84	0.75	0.71
Gmelinite	1.38	0.10	0.70
Offretite	1.33	0.76	0.68
CoAPO-50	1.28	0.90	0.61
Cancrinite	1.28	0.51	0.59
VPI-5	1.90	0.84	1.21

### A. Geometrical Constraints

The geometrical constraints imposed by the host determines the organization of the dyes. We focus on systems consisting of dye molecules in hexagonally arranged linear channels. Materials providing such channels are reported in Table 1. We investigate a cylindrical shape as illustrated in Fig. 5. The primitive vector  $c$  corresponds to the channel axis while the primitive vectors  $a$  and  $b$  are perpendicular to it enclosing an angle of  $60^\circ$ . The channels run parallel to the central axis of the cylinder [62]. The length, and the diameter of the cylinder are  $l_z$ , and  $d_z$ , respectively. The following concepts and definitions cover situations we found to be important. They refer to systems as illustrated in Fig. 1.

(a) The number of parallel channels  $n_{ch}$  of a hexagonal crystal which can be approximated by a cylinder of diameter  $d_z$  is given by

$$n_{ch} = \frac{\left(\frac{d_z}{2}\right)^2 \pi}{|a|^2 \sin(60)} = \frac{\pi}{2\sqrt{3}} \left(\frac{d_z}{|a|}\right)^2 \quad (1)$$

which can be approximated for zeolite L as

$$n_{ch} \simeq 0.267(d_z)^2 \quad (2)$$

where  $d_z$  is in units of nm. This means that a zeolite L of 500 nm diameter gives rise to about 67'000 parallel channels.

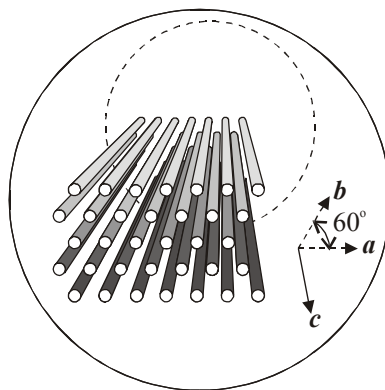


**Figure 5.** Schematic view of some channels in a hexagonal zeolite crystal with cylinder morphology.

**(b)** The dye molecules are positioned at sites along the linear channels. The length of a site is equal to a number  $n_s$  times the length of  $c$ , so that one dye molecule fits into one site. Thus  $n_s$  is the number of unit cells which form a site which we name  $n_s$ -site.  $n_s$  depends on the size of the dye molecules and on the length of the primitive unit cell. As an example a dye with a length of  $\approx 1.5$  nm in zeolite L requires two primitive unit cells, therefore  $n_s$  is equal to 2 and the sites are called 2-site. The sites form a new (pseudo) Bravais lattice with the primitive vectors  $a$ ,  $b$ , and  $n_s c$  in favorable cases.

**(c)** Different types of sites exist. Those occupied with luminescent dye molecules are marked with small letters. Capital letters are reserved for traps which may or may not be luminescent. Per crystal, the number of sites available for dye molecules is  $I_{max}$  and the number of sites available for traps is  $I_{max}$ . Equivalent  $n_s$ -sites have the same geometrical properties. Dye molecules in equivalent sites  $i$  are assumed to be equivalent. The same is valid for traps.

**(d)** In general only dye molecules with a large electronic transition dipole moment  $\mu_{S_1 \leftarrow S_0}$  are considered in this account. This means that the  $S_1 \leftarrow S_0$  transition is of  $\pi^* \leftarrow \pi$  type.

**(e)** Equivalent  $n_s$ -sites  $i$  have the same probability  $p_i$  to be occupied by a dye molecule. The occupation probability  $p$  is equal to the ratio between the occupied and the total number of equivalent sites. The number of unit cells  $n_{uc}$  is controlled by the host while  $n_s$  is determined by the length of the guest. This means that  $p$  relies on purely geometrical (space filling) reasoning and that the dye concentration per unit volume of a zeolite crystal can be expressed as a function of  $p$  as follows:

$$c(p) = \frac{\rho_Z}{m_Z} \frac{p}{n_s} \quad (3)$$

where  $\rho_Z$  is the density and  $m_Z$  the mass of the zeolite crystal. In cases where cationic dye molecules are inserted by ion exchange,  $p$  is proportional to the exchange degree  $\theta$ , which is defined as the ratio of dye molecules and exchangeable cations. The relation between the exchange degree  $\theta$  and the occupation probability  $p$  is given by [26]:

$$p = n_s n_{M^+} \theta \quad (4)$$

where  $n_{M^+}$  is the number of exchangeable cations per unit cell. The occupation probability  $p_I$  of sites  $I$  is treated in an analogous way. Zeolite literature often refers to the equivalent

fraction of exchanging species  $\theta_z$  [7]. It is defined as the number of inserted cations divided by the total numbers of cations in the zeolite. In simple cases the relation between the occupation probability and  $\theta_z$  is obvious [63]. The occupation probability is more general, however, and more useful for our purpose.

(f) Each equivalent site  $i$  of a given crystal has the same probability  $P_i$  of being occupied by an electronically excited molecule, immediately after irradiation with a Dirac pulse. The excitation probability  $P_i$  of site  $i$  is the  $i$ th element of a vector  $\mathbf{P}$  which we call excitation distribution among the sites. We distinguish between the low intensity case in which at maximum one dye molecule per crystal is in an electronically excited state and cases where two or more molecules in a crystal are in the excited state. Where not explicitly mentioned we refer to the low intensity case.

(g) We consider the case where the sites form a Bravais lattice. This means that the position  $R_i$  of an  $n_s$ -site  $i$  can be expressed by the primitive vectors  $\mathbf{a}$ ,  $\mathbf{b}$ , and  $n_s \cdot \mathbf{c}$  of the hexagonal lattice and the integers  $n_{a,i}$ ,  $n_{b,i}$  and  $n_{c,i}$ :

$$\mathbf{R}_i = n_{a,i}\mathbf{a} + n_{b,i}\mathbf{b} + n_{c,i}n_s\mathbf{c} \quad (5)$$

This description is always precise for  $n_s = 1$ . Because it greatly simplifies the description, we will use it as an approximation for  $n_s > 1$ , too. Deviations from a more precise statistical treatment are probably small in general because even small crystals consist of a large number of sites so that differences may cancel. It is, however, not yet clear under what conditions this assumption breaks down. Anyhow, in this simplified description sites with equal  $n_c$  belong to slabs cut perpendicular to the  $\mathbf{c}$  axis. This is illustrated in Fig. 6.

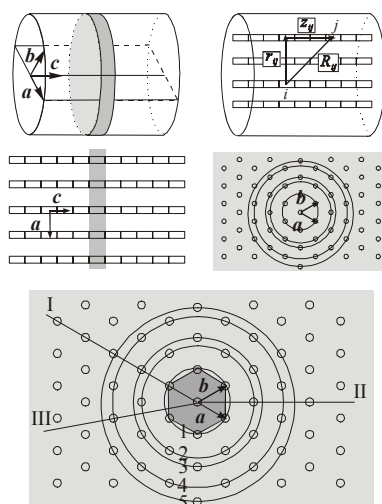


**Figure 6.** Geometrical situation. The sites are marked by rectangles. *Top:* Primitive vectors  $\mathbf{a}$ ,  $\mathbf{b}$ , and  $\mathbf{c}$ . Definition of the distances  $R_{ij}$ ,  $r_{ij}$  and  $z_{ij}$  between sites  $i$  and  $j$ . *Middle, left:* Cut through the center of the hexagonal crystal with cylinder morphology along  $\mathbf{a}$  and  $\mathbf{c}$ . The sites of the shaded area belong to one slab. *Middle, right:* Cut vertical to  $\mathbf{c}$ . The channels indicated by circles are arranged on rings around the central channel because of the hexagonal symmetry. *Bottom:*  $r_I$ ,  $r_{II}$  and  $r_{III}$  are the distances from one channel to the next channel along lines I, II and III.

The first slab is situated at the front and the last slab on the back of the cylinder. The total number of slabs  $n_{sb}$  depends on the length  $l_z$  of the cylindrical microcrystal.



$$n_{sb} = \frac{l_z}{n_s |\mathbf{c}|} \quad (6)$$

The thickness of a slab is  $n_s \cdot |\mathbf{c}|$ .

**(h)** The distance  $r$  between a channel  $(n_a, n_b)$  and the central channel is given by  $r = |n_a \mathbf{a} + n_b \mathbf{b}|$ . The channels are characterized by the numbers  $(n_a, n_b)$ , hence, sites with the same  $(n_a, n_b)$  values belong to the same channel.  $n_a$  and  $n_b$  are both equal to zero for the central channel, which coincides with the cylinder axis. The possible range of  $(n_a, n_b)$  is limited by the condition  $|n_a \mathbf{a} + n_b \mathbf{b}| \leq d_z/2$ . Because of the hexagonal symmetry,  $\mathbf{a}$  and  $\mathbf{b}$  have equal lengths and the angle between  $\mathbf{a}$  and  $\mathbf{b}$  is  $60^\circ$ . The length  $r$  of the vector  $n_a \mathbf{a} + n_b \mathbf{b}$  is therefore given by:

$$r = |\mathbf{a}| \sqrt{(n_a + n_b \cos 60^\circ)^2 + (n_b \sin 60^\circ)^2} = |\mathbf{a}| \sqrt{n_a^2 + n_a n_b + n_b^2} \quad (7)$$

Rings consisting of six channels can be formed, due to the hexagonal symmetry, as illustrated in Fig. 6. The six channels on one ring all have the same distance from the center  $(0,0)$ . A transformation can be given to go from one channel on a ring to the other five channels. Two, three or more 6-rings can be located on the same circle but displaced by a certain angle, due to the hexagonal symmetry. The tubes of each of these 6-rings, however, behave in the same way. The distances  $r_I$ ,  $r_{II}$  and  $r_{III}$  can be expressed as:  $r_I = n\mathbf{a}$ ,  $r_{II} = 3^{0.5}n\mathbf{a}$ , and  $r_{III} = (n^2 + n + 1)^{0.5}\mathbf{a}$ , where  $n = 1, 2, 3, \dots$

**(i)** The probability for energy transfer between two sites  $i$  and  $j$  strongly depends on the vector  $\mathbf{R}_{ij}$  which is characterized by

$$\mathbf{R}_{ij} = (n_{a,i} - n_{a,j})\mathbf{a} + (n_{b,i} - n_{b,j})\mathbf{b} + (n_{c,i} - n_{c,j})n_s \mathbf{c} \quad (8)$$

$$R_{ij} = \sqrt{r_{ij}^2 + z_{ij}^2} \quad (9)$$

where  $r_{ij}$  and  $z_{ij}$  are the distances between the channels and the slabs to which the two sites belong. They correspond to the distances between the sites parallel and perpendicular to  $\mathbf{c}$ , respectively.  $R_{ij}$ ,  $z_{ij}$ , and  $r_{ij}$  are indicated in Fig. 6.

$$r_{ij} = |\mathbf{a}| \sqrt{(n_{a,i} - n_{a,j})^2 + (n_{a,i} - n_{a,j})(n_{b,i} - n_{b,j}) + (n_{b,i} - n_{b,j})^2} \quad (10)$$

$$z_{ij} = n_s |\mathbf{c}| (n_{c,i} - n_{c,j}) \quad (11)$$

**(j)** In crystals containing more than one type of dye, the definitions and concepts must be adapted correspondingly.

## B. Inner and Outer Surface of the Zeolite Nanocrystals

Cationic and neutral dyes have the tendency to adsorb at the inner and at the outer surface of the zeolite crystals. It is to be expected that the affinity of molecules to the coat and the base area differs. The coat and the base area of a good zeolite L material are nicely illustrated on the left and right side, respectively, of Fig. 7. The number of molecules needed to form a monolayer  $n_D$  on a cylinder of surface  $A_Z$  is:

$$n_D = \frac{A_Z}{A_D} \quad (12)$$

where  $A_D$  is the surface required by a dye molecule. It depends not only on its size but also on the specific arrangement of the molecules in the monolayer.

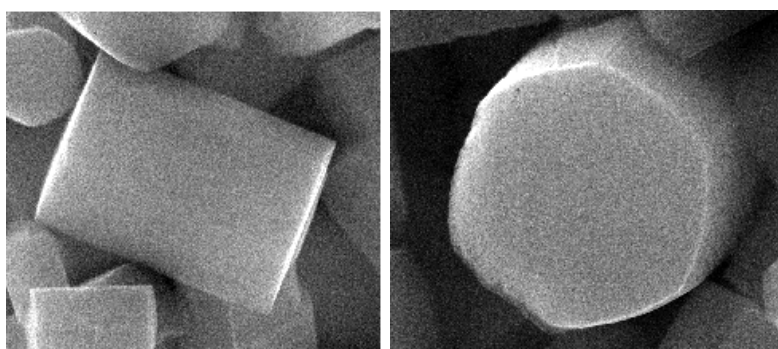


**Figure 7.** Side and top view of zeolite L crystals. The length of the left crystal is about 950 nm, the diameter of the right crystal is about 850 nm.

It is often useful to express  $n_D$  in terms of the Volume  $V_Z$  and of the density  $\rho_Z$  of a zeolite crystal:

$$A_Z = 2\pi\left(\frac{d_Z}{2}\right)^2 + \pi d_Z l_Z \quad (13)$$

$$V_Z = \pi\left(\frac{d_Z}{2}\right)^2 l_Z = \frac{m_Z}{\rho_Z} \quad (14)$$

where  $d_Z$ ,  $l_Z$  and  $m_Z$  are the diameter, the length and the mass of the zeolite crystal. This leads to the following expression for  $n_D$ :

$$n_D = \frac{2}{A_D} \left( \frac{V_Z}{l_Z} + \sqrt{\pi V_Z l_Z} \right) \quad (15)$$

or:

$$n_D = \frac{\pi}{A_D} \left( \frac{d_Z^2}{2} + d_Z l_Z \right) \quad (16)$$

We compare  $n_D$  with the number of unit cells  $n_{uc}$  of the crystal. The number of unit cells per channel is equal to its length divided by the length of the unit cell  $c$ . Using eq. (1) we can write:

$$n_{uc} = n_{ch} \frac{l_Z}{|c|} = \frac{\pi}{2\sqrt{3}} \left( \frac{d_Z}{|a|} \right)^2 \frac{l_Z}{|c|} \quad (17)$$

From this follows the ratio of  $n_{uc}$  and  $n_D$ :

$$\frac{n_{uc}}{n_D} = \frac{d_Z l_Z}{d_Z + 2l_Z} \frac{A_D}{\sqrt{3} |a|^2 |c|} \quad (18)$$

Applying the values of  $a$  and  $c$  for zeolite L leads to:

$$n_{uc} = 0.357 d_Z^2 l_Z \quad (19)$$

$$\frac{n_{uc}}{n_D} = 0.227 A_D \frac{d_Z l_Z}{d_Z + 2l_Z} \quad (20)$$

where  $d_Z$  and  $l_Z$  are in units of nm. Hence, a zeolite L cylinder of 100 nm length and diameter consists of 2670 channels and 35'700 unit cells, one of 1000 nm length and 600 nm diameter consists of 96'400 channels and  $1.28 \cdot 10^6$  unit cells. For a molecule that occupies two unit cells,  $A_D$  is in the order of 1.4 nm<sup>2</sup>. This gives a ratio  $\frac{n_{uc}}{2n_D}$  of 5.3 for the small crystals and 36.7 for the larger ones. From this it is clear that the number of molecules which in principle can form a monolayer at the outer surface is in the same order of magnitude as the number of sites inside of the material, despite of its high porosity. Obviously the smaller the crystals are, the more important it is to distinguish between molecules at the outer and at the inner surface of the material. Experiments to distinguish between molecules at the inner and outer surface make use of geometrical and electrostatic constraints of the negatively charged zeolite framework. The same principle is used to remove or to destroy unwanted molecules at the outer surface [53].

Because we are studying an anisotropical system where energy transport is possible along the channels and from one channel to another one, it is useful to consider the ratio  $R_{ch/site}$  between the number of parallel channels and the number of  $n_s$ -sites in a channel:

$$R_{ch/site} = \frac{n_{ch}}{l_Z / (n_s c)} = \frac{\pi}{2\sqrt{3}} \left( \frac{d_Z}{a} \right)^2 \frac{n_s c}{l_Z} \quad (21)$$

Applying this to zeolite L gives:

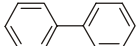
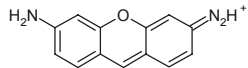
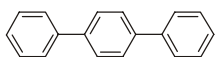
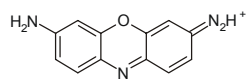
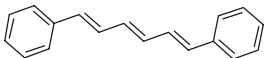
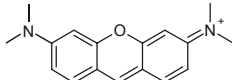
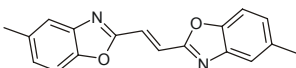
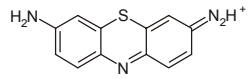
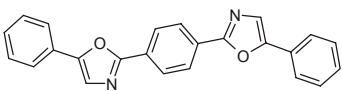
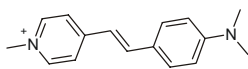
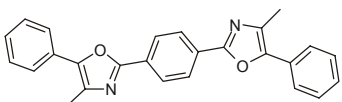
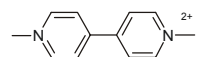
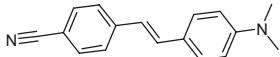
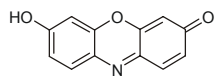
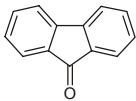
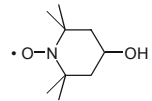
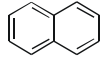
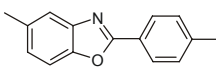
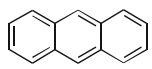
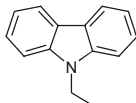
$$R_{ch/site} = 0.2 n_s \frac{d_Z^2}{l_Z} \quad (22)$$

where  $d_Z$  and  $l_Z$  are in units of nm. This means for example that  $R_{ch/site}$  is equal to 144 for a crystal of 1000 nm length and 600 nm diameter and a dye which occupies two unit cells.

### C. The Dyes

Representative dyes we have inserted in zeolite L are listed in Table 2. Many of them lead to strongly luminescent materials. Some exceptions are Fluorenone, MV<sup>2+</sup>, ResH and Hydroxy-TEMPO.

**TABLE 2** Dye molecules and abbreviations (\* taken from [64])

BP			Py <sup>+</sup>
<i>p</i> TP			Ox <sup>+</sup>
DPH			PyGY <sup>+</sup>
MBOXE			TH <sup>+</sup>
POPOP			DSMI <sup>+</sup>
DMPOPOP			MV <sup>2+</sup>
DSC			ResH
Fluorenone			Hydroxy-TEMPO
Naphtalene*			PBOX
Anthracene*			N-Ethylcarbazole*

We distinguish between the four different orientations **1**, **2**, **3**, and **4** of molecules in the channels explained in Fig. 8. Molecules with a length of more than two unit cells have no other choice but to align along the channels, see also Figures 3 and 4. They correspond to case **1** of Fig. 8, if their first  $\pi^* \leftarrow \pi$  electronic transition moment coincides with their long axis. Molecules which are shorter than two unit cells may align as illustrated by the pictures **2** or **3**. **4** indicates that the long axis of the molecule and the transition moment do not coincide. The long molecules **1** will arrange as shown in the middle of Fig. 8, if their space filling is such, that any overlap is prohibited. This means that no electronic interaction occurs and that

the material will behave as expected from ordered monomeric molecules of very high concentration in a crystal. More flexible and thinner molecules have the option to arrange as indicated at the bottom of Fig. 8. In this case electronic interaction between the molecules occurs with the corresponding consequences.

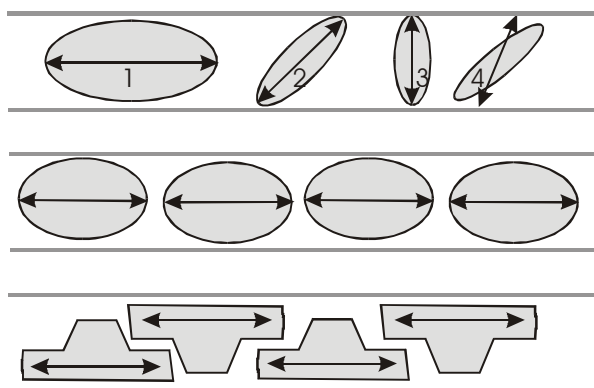


**Figure 8.** Simplified view of different orientations and two arrangements of molecules in the channels of zeolites. *Upper:* four representative orientations of molecules and their electronic transition moments, indicated by the double arrow. *Middle:* orientation of large molecules which align parallel to the channel axis and which have no electronic interaction because of their size and shape. *Bottom:* orientation of large molecules which align parallel to the channel axis and which have some electronic interaction because of their shape.

While DMPOPOP is a case for which orientation **1** and the arrangement in the middle of Fig. 8 are expected to hold,  $MV^{2+}$  is a candidate for orientation **2**, as illustrated in Fig. 9.

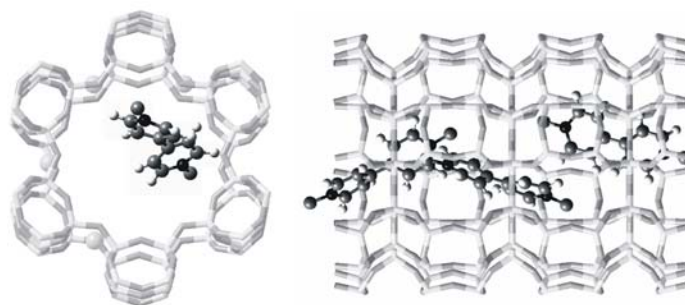


**Figure 9.** Location of  $MV^{2+}$  in zeolite L based on x-ray powder diffraction data [25]. *Left:* View along the channel axis showing the position and orientation of a molecule. *Right:* Side view of the channel depicting the arrangement of the molecules.

Optical fluorescence microscopy is a powerful and sensitive method for obtaining information about the orientation of luminescent dye molecules in small crystals. We show in Fig. 10 unpolarized and linearly polarized fluorescence of two perpendicularly lying zeolite L crystals loaded with DSC. The exciting light was not polarized. Obviously, the material is optically very anisotropic. Since the atom to atom length of DCS is about 15 Å and therefore corresponds to almost exactly two unit cells, we conclude that it orients in the channels according to case **1** in Fig. 8. Other molecules for which we found the same behavior are POPOP, DMPOPOP, DPH, and MBOXE. The optical properties of these materials can be

illustrated by means of Fig. 11 where on the right some individual channels are depicted. Surprisingly, case 4 was observed for  $\text{Ox}^+$  loaded zeolite L. We refer to [54] for details.



**Figure 10.** Fluorescence microscopy picture of two 1500 nm long zeolite L crystals containing DSC. Excitation with unpolarized light at 480 nm. *Left:* unpolarized observation. *Middle and Right:* linearly polarized observation. The arrows indicate the polarization direction.

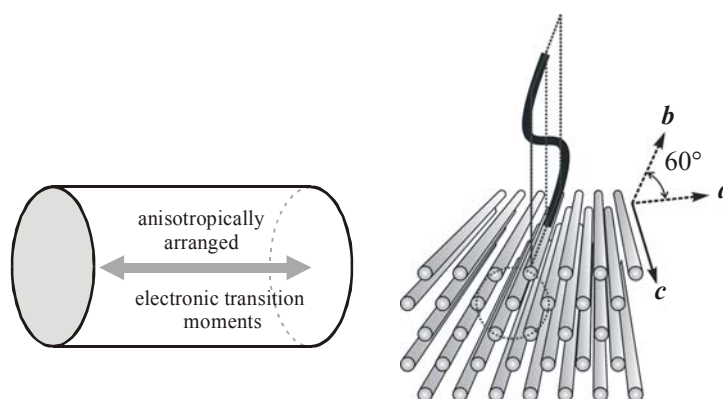


**Figure 11.** Schematic view of a zeolite L crystal loaded with type 1 (Fig. 8) dyes with electronic transition moments aligned along the axis of the channels. *Left:* side view of the morphology, size and optical anisotropy of the material. *Right:* front view of a few individual dye-filled channels. The polarization of absorbed and emitted light is indicated.

#### D. Three-dye Antenna

We recently reported the preparation of sophisticated bipolar three-dye photonic antenna materials for light harvesting and transport [22]. The principle is illustrated in the center of Fig. 12, surrounded by fluorescence microscopy pictures of antenna crystals of about 1.5  $\mu\text{m}$  length. Zeolite L microcrystals of cylinder morphology are used as host for organizing several thousand dyes as monomers into well-defined zones. The enlarged section schematically shows the organization of dye molecules at the domain boundary between dye2 and dye3. The microscopy pictures demonstrate the antenna behavior: They show the red fluorescence of dye3, located at both ends of the crystals, after selective excitation of the blue dye1 in the middle.

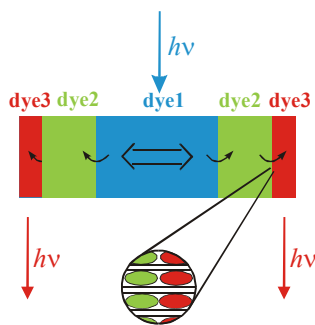


**Figure 12.** Principle of a bipolar three-dye photonic antenna. A crystal is loaded with a blue, a green and a red emitting dye. After selective excitation of the blue dye in the middle, energy transfer takes place to both ends of the crystal where the red dye fluoresces.

The idea that it should be possible to prepare such a sophisticated material emerged from the following qualitative observations, made by means of a standard optical microscope equipped with polarizers and an appropriate set of filters [55]. A side view of a zeolite L crystal of about  $1.5\ \mu\text{m}$  is illustrated in Fig. 13. We observed in this material the process of insertion of  $\text{Py}^+$  and in a second step of  $\text{Ox}^+$  into the channels, out of an aqueous suspension of zeolite L crystals containing dissolved  $\text{Py}^+$  and  $\text{Ox}^+$ , respectively. The zeolite L samples **2-4** were excited with light of 470-490 nm where only  $\text{Py}^+$  absorbs. In **2** we see how  $\text{Py}^+$  penetrates the cylinder from both sides in the direction of the cylinder axis. After an exchange of 5 min under reflux the crystal ends show the typical green fluorescence of  $\text{Py}^+$ , while the section in the middle remains dark. The fluorescence is seen over the whole crystal after 2 h exchange, **3**. The dye molecules have moved towards the center now, but the fluorescence at the ends still appears to be more intense. The result after additional exchange with  $\text{Ox}^+$  for 2 h is illustrated in **4** and **5**. It leads to crystals, which show the green fluorescence of  $\text{Py}^+$  in the center and the fluorescence of  $\text{Ox}^+$  at both ends. The yellow color seen in **4** is due to the mixing of the green  $\text{Py}^+$  and the red  $\text{Ox}^+$  fluorescence.  $\text{Ox}^+$  was not excited directly, but via energy transfer from excited  $\text{Py}^+$  molecules. After specific excitation of  $\text{Ox}^+$  at 545-580 nm, picture **5**, only the red fluorescence at both ends is visible while the middle part of the zeolite L crystal remains dark. This nicely demonstrates that a stacking of  $\text{Py}^+$  in the middle and  $\text{Ox}^+$  at both ends of the cylinders is achieved. The electronic absorption and emission spectra of  $\text{Py}^+$  and  $\text{Ox}^+$  are reported in Fig. 14. The maxima of the absorption and emission spectra of the dyes inside of the zeolite are slightly shifted to longer wavelengths and they are more structured than those recorded in water.

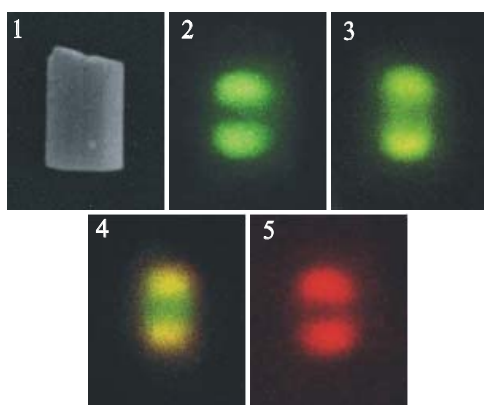


**Figure 13. 1:** Electron microscopy picture of a zeolite L crystal with a length of about 1.5  $\mu\text{m}$ . **2-5:** True color fluorescence microscopy pictures of dye loaded zeolite L crystals. **2-4:** Fluorescence after excitation of only  $\text{Py}^+$ . **2** after 5 min exchange with  $\text{Py}^+$ , **3** after 2 h exchange with  $\text{Py}^+$ , **4** after additional 2 h exchange with  $\text{Ox}^+$ . **5:** The same as **4** but after specific excitation of only  $\text{Ox}^+$ .

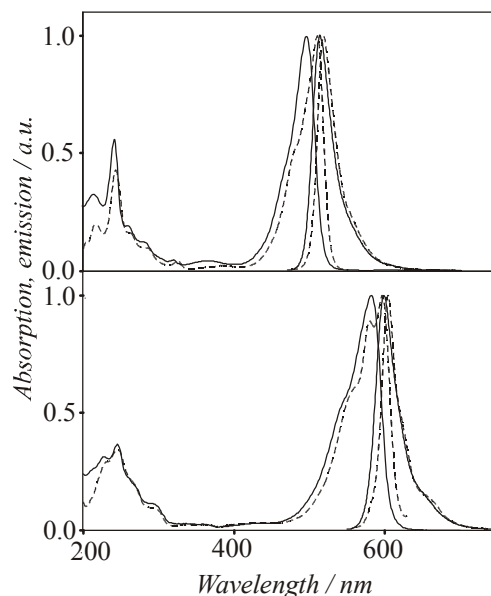


**Figure 14.** Electronic absorption and emission spectra of  $\text{Py}^+$  and of  $\text{Ox}^+$  in aqueous solution (solid) and in zeolite L (dashed). *Upper:*  $\text{Py}^+$  absorption and fluorescence ( $\lambda_{\text{ex}}$ : 460 nm) spectra in aqueous solution and excitation ( $\lambda_{\text{em}}$ : 560 nm) and fluorescence ( $\lambda_{\text{ex}}$ : 460 nm) spectra in zeolite L suspension. *Lower:*  $\text{Ox}^+$  absorption and fluorescence ( $\lambda_{\text{ex}}$ : 560 nm) spectra in aqueous solution and excitation ( $\lambda_{\text{em}}$ : 640 nm) and fluorescence ( $\lambda_{\text{ex}}$ : 560 nm) spectra in zeolite L suspension.

The general concept of the synthesis of sandwich materials is illustrated in Fig. 15. In our first report on this [22] we first inserted a neutral dye1 from the gas phase, filling the channels to the desired degree. It was possible to find conditions to insert a cationic dye2 from an aqueous suspension, despite of the fact that neutral dyes are usually displaced by water molecules. This process can be well controlled so that a specific desired space is left for the third dye3 to be inserted. It is also possible to insert first a cationic dye and then a neutral one or to use other combinations. The principle can be extended to more than three different dyes.



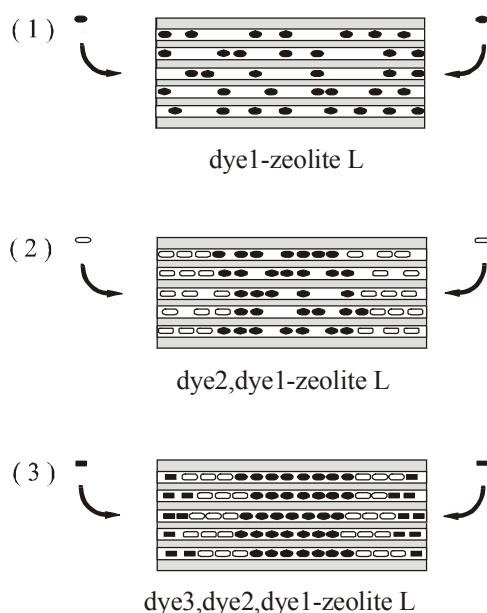


**Figure 15.** Successive insertion of three different dyes into the channels of a zeolite L crystal to form a sandwich material.

A nice example which demonstrates the stacking of a neutral and a cationic dye, POPOP and  $\text{Py}^+$ , is illustrated in Fig. 16 on zeolite L crystals of about  $2 \mu\text{m}$  length. We show the luminescent behavior of two selected crystals, which were filled in the middle part by POPOP, and at both ends with a thin layer of  $\text{Py}^+$ . The latter is visible in **1**, where  $\text{Py}^+$  is excited selectively at 470-490 nm. The characteristic green fluorescence of the  $\text{Py}^+$  located at both ends of the crystals is observed. The three other pictures show mainly the luminescence of POPOP. **2**: Excitation at 330-385 nm. The POPOP fluorescence is strong, because of its much larger concentration, so that the green  $\text{Py}^+$  emission can hardly be distinguished. **3** and **4**: The same as **2** but observed by means of a polarizer, the direction of which is shown by the arrows. The result is obvious: strong POPOP emission in direction of the  $c$ -axis, weak emission perpendicular to it. The weak emission at both ends of the crystals in pictures **3** (upper) and **4** (lower) are due to the  $\text{Py}^+$  emission, which is nearly perpendicular to that of the POPOP. Its appearance is mainly due to energy transfer from excited POPOP.

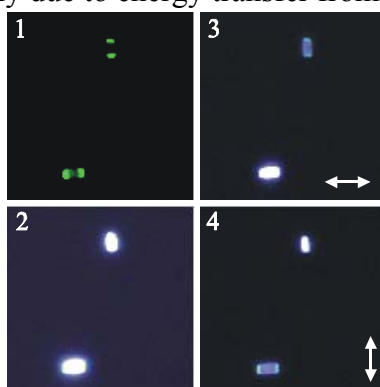


**Figure 16.** True color microscopy pictures of  $\text{Py}^+$ , POPOP-zeolite L of crystals of about  $2 \mu\text{m}$  length. **1** Specific excitation of  $\text{Py}^+$  at 470-490 nm. **2** Excitation at 330-385 nm. **3** and **4** show the same as **2** but after observation with a polarizer. The polarization is indicated by the arrows.

From this one might assume that the stacking of dye molecules in the channels should always be easily visible by means of optical microscopy, provided that the crystals are large enough. However, this is not the case because special kinetic conditions must hold so that the mean phase boundaries lie perpendicular to the long axis. Other conditions lead to bent mean phase boundaries. The two cases are explained in Fig. 17 for a two dye system,  $D_1$  and  $D_2$ . The upper case is easy to analyze in an optical microscope, see e.g. Fig. 16. The lower case is more difficult to detect. The simplest way to obtain the necessary information in this case is to use a thick region with dense filling of  $D_2$  dyes, so that the two  $D_1$  regions appear separated despite of the strong bending of the mean phase boundary.

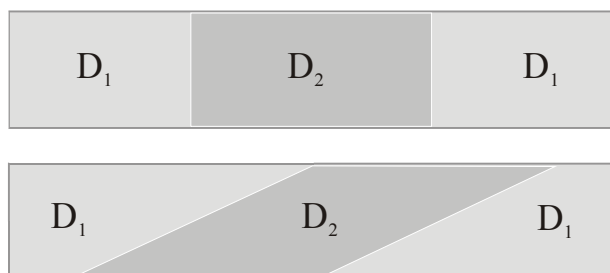


**Figure 17.** Two kinds of mean phase boundaries of a two dye,  $D_1$  and  $D_2$ , sandwich system. The phase boundaries are sorted according to their distance from the front and back.

Fig. 18 shows fluorescence microscopy images of a bipolar three-dye antenna material with POPOP in the middle, followed by  $Py^+$  and then by  $Ox^+$ . The different color regions which can be observed in this simple experiment are impressive. The red color of the luminescence (1) disappears, when the crystal is observed through a polarizer parallel to the crystal axis while the blue emission disappears when turning the polarizer by  $90^\circ$ . This material is very stable and is easy to handle.

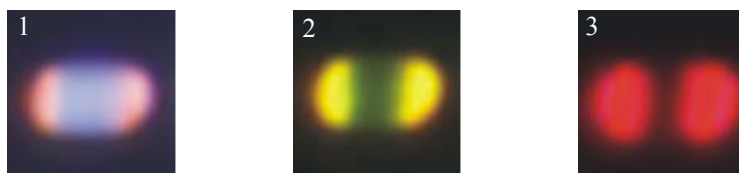


**Figure 18.** Fluorescence microscopy images of an  $Ox^+, Py^+, POPOP$ -zeolite L crystal of 2000 nm length upon selective excitation of **1** POPOP at 330-385 nm, **2**  $Py^+$  at 470-490 nm and **3**  $Ox^+$  at 545-580 nm.

## E. The Stopcock Principle

The dye loaded materials described so far exhibit a number of shortcomings. In particular the stability is unsatisfactory because the dyes can migrate out of the channels resulting in a depletion of the dye loaded zeolite material. Moreover the task of external trapping of excitation energy or - conversely - of injecting energy at a specific point of the photonic antenna, the realization of a one-directional photonic antenna and the coupling to a specific device are challenging.

The stability problem can be solved just by adding a layer of unspecific closure molecules. External trapping and injection of quanta is more demanding. The general approach we are using to solve this problem is to add a "stopcock" as illustrated in Fig. 19. These closure molecules have an elongated shape consisting of a head moiety and a tail moiety, the tail moiety having a longitudinal extension of more than the dimension of a crystal unit cell along the *c*-axis and the head moiety having a lateral extension that is larger than the channel width and will prevent the head from penetrating into the channel. The channels are therefore terminated in generally plug like manner.

Tails can be based on organic and silicon organic backbones. Four types of tails play a role, depending on the desired properties. (i) Non reactive tails. (ii) Tails which can undergo an isomerization after insertion under the influence of irradiation, heat or a sufficiently small reactive. (iii) Reactive tails which can bind to molecules inside of the channels. (iv) Luminescent tails, which have the advantage of being protected by the zeolite framework.

The heads of the stopcock molecules must be large enough so that they cannot enter the channels. They should fulfill the stability criteria imposed by a specific application and it should be possible to functionalize them in order to tune the properties of surface (e.g. the wetting ability, refractive index matching, reactivity). Heads can consist of organic, silicon organic, but also of coordination compounds. In some cases it is desirable to use heads which bear reactive "arms" so that in an additional step they can interact with each other to form a "monolayer polymer".

*Acceptor-heads* should in general be strongly luminescent molecules with a large spectral overlap with the donor molecules located inside of the channels. Since luminescence is quenched by dimerization the structure must be such that the chromophores do not interact electronically with each other. Nearly all strongly luminescent organic chromophores can be considered since it is always possible to attach inert e.g. aliphatic groups so that the head cannot enter the channels. In reality many of these chromophores will turn out to be less interesting because of stability, shape, toxicity etc. A very interesting aspect of the principle discovered by us is that the head can be chosen or functionalized in order to realize the desired properties. The difference of the *donor-heads* with respect to the acceptors is that they must be able to transfer their excitation energy (by a radiationless process, in general dipole-dipole coupling) to acceptors located inside of the channels.

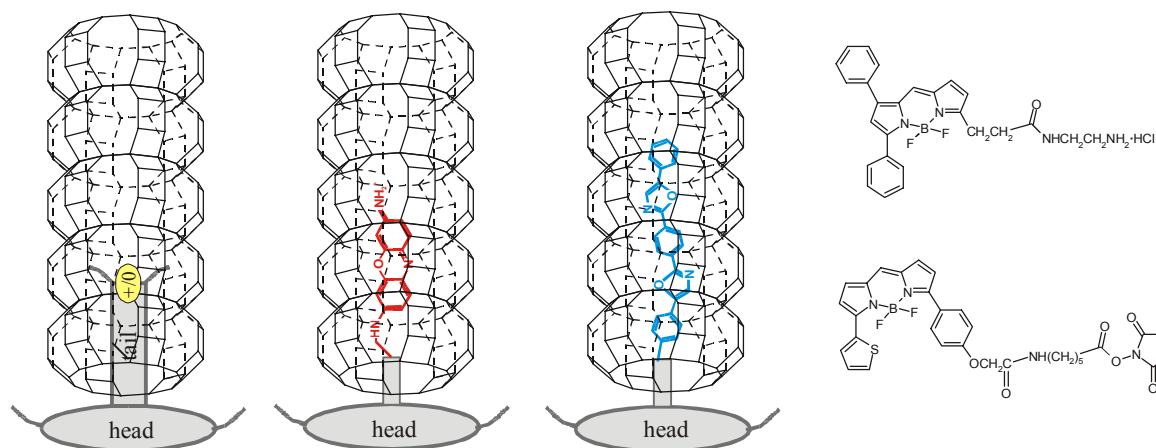


**Figure 19.** *Left:* Typical shape of a head-tail molecule acting as an injector-, acceptor-, or simply as a stopcock. The positive charge is desirable for anionic framework hosts, but not necessary. Reactive groups may help to fix the stopcock. *Middle:* Fluorescent molecules which already have been inserted in zeolite L could be modified with an inert head. *Right:* Examples of molecules which could be used as stopcocks with a fluorescent head.

### III. TRANSFER OF ELECTRONIC EXCITATION ENERGY

Important transfer and transformation processes of electronic excitation energy which can take place in dye loaded zeolite materials are:

- absorption/emission of a photon
- transformation into chemical energy and the reverse
- transformation into heat
- radiationless and radiative transfer to an acceptor
- stimulated emission
- upconversion

Energy transfer processes in which free photons exist as intermediates are sometimes referred to as "trivial" transfer mechanism. This term is misleading in the sense that such processes e.g. in combination with internal reflection can cause very complex and interesting phenomena [3, 65-67]. Radiationless energy transfer processes have been studied extensively since the pioneering work of Förster [68, 69] and Dexter [70], see e.g. refs. [40, 67, 71-73]. Here we concentrate on the description of one photon processes, specifically with respect to radiationless energy transfer processes.

#### A. Radiationless Energy Transfer

Excitation transfer requires some interaction between unexcited and excited molecules  $M$  and  $M^*$ , respectively. We denote the two molecules under consideration as  $M$  and  $M'$ . The interaction can then be expressed as occurring between the two configurations  $MM^*$  and  $M^*M'$ :

$$\psi_i = \frac{1}{\sqrt{2}} (\psi_{M^*}^{(1)} \psi_M^{(2)} - \psi_{M^*}^{(2)} \psi_M^{(1)}) \quad (23)$$

$$\psi_f = \frac{1}{\sqrt{2}}(\psi_M^{(1)} \psi_{M^*}^{(2)} - \psi_M^{(2)} \psi_{M^*}^{(1)}) \quad (24)$$

where  $i$  and  $f$  denote the initial and final state, respectively, and (1) and (2) refer to electrons. Using  $H'$  for the interaction Hamiltonian, the interaction energy  $\beta$  is

$$\beta = \frac{u}{2} - \frac{ex}{2} \quad (25)$$

where  $u$  denotes the Coulomb interaction and  $ex$  the exchange interaction:

$$u = \langle \psi_{M^*}^{(1)} \psi_{M'}^{(2)} | H' | \psi_M^{(1)} \psi_{M'^*}^{(2)} \rangle \quad (26)$$

$$ex = \langle \psi_{M^*}^{(1)} \psi_{M'}^{(2)} | H' | \psi_M^{(2)} \psi_{M'^*}^{(1)} \rangle \quad (27)$$

If more than two electrons should be involved, these expressions can be extended accordingly. The transfer rate  $k_{el}$  for electronic excitation energy

$$M^*M' \rightleftharpoons MM'^* \quad (28)$$

can be expressed by means of the Golden Rule as follows:

$$k_{el} = \frac{2\pi}{\hbar} \beta^2 \rho \quad (29)$$

where  $\rho$  is the density of states.

We consider situations for which the orbital overlap between  $M$  and  $M'$  is negligible, this means situations as depicted in the upper and middle part of Fig. 8. This makes sense because we focus on strongly luminescent materials. In general, orbital overlap causes fast radiationless decay for organic molecules as e.g. observed in dimers [56, 57]. The exchange part  $ex$  vanishes in absence of orbital overlap. In this case the initial and the final states can be simply expressed as:

$$\psi_i = \psi_{M^*} \psi_{M'} \quad (30)$$

$$\psi_f = \psi_M \psi_{M'^*} \quad (31)$$

Following the arguments of Förster [74] we distinguish between strong, medium and weak coupling. Weak interaction means that the interaction energy  $u$  is less than the vibrational bandwidth. In this case energy transfer must be treated as a non-radiative transition between two configurations with continuous energy and the so called Förster equation as used in the next section can be derived [68-70, 72].

## B. Förster energy transfer in dye loaded zeolite L

Using the geometrical concepts explained in section II-A it is convenient to express the rate constant for energy transfer from an excited donor  $i$  to an acceptor  $j$  as follows [75]:

$$k_{ij}^F = \frac{9 \ln(10)}{128 \pi^5 N_A \eta^4} \frac{\phi_i}{\tau_i} J_{ij} G_{ij} p_i p_j \quad (32)$$

$$k_{ij}^F = k_{ij}^{ET} \quad \text{when sites } i \text{ and } j \text{ are occupied with molecules of different kinds} \quad (33)$$

$$k_{ij}^F = k_{ij}^{EM} \quad \text{when sites } i \text{ and } j \text{ are occupied with molecules of the same kind} \quad (34)$$

where  $\phi_i$  and  $\tau_i$  [s<sup>-1</sup>] are the fluorescence quantum yield and the intrinsic fluorescence lifetime of the donor,  $N_A$  [mol<sup>-1</sup>] is Avogadro's number,  $\eta$  is the refractive index of the medium,  $G_{ij}$  [Å<sup>-6</sup>] expresses the geometrical constraints of the sites in the crystal and the relative ordering of the electronic transition moments,  $p_i$  and  $p_j$  are the occupation probabilities of the sites with excited donors  $i$  and acceptors  $j$  in the ground state, and  $J_{ij}$  [cm<sup>3</sup>M<sup>-1</sup>] is the spectral overlap integral between the normalized donor emission and the acceptor absorption spectra.  $k_{ij}^{EM}$  and  $k_{ij}^{ET}$  are the rate constants for energy migration from a site  $i$  to a site  $j$  and energy transfer to a trap  $J$ , respectively. Eq. 32 refers to non overlapping sites and translational symmetry of the sites. It is possible to generalize it by averaging over different site distributions. This is not done here. Expressing  $G_{ij}$  as a function of the donor  $i$  to acceptor  $j$  distance  $R_{ij}$  and the relative orientation of the electronic transition moments ( $\mu_{S_1 \leftarrow S_0}$ ) <sub>$i$</sub>  and ( $\mu_{S_1 \leftarrow S_0}$ ) <sub>$j$</sub>  we write:

$$G_{ij} = \frac{\kappa_{ij}^2}{R_{ij}^6} \quad (35)$$

$\kappa_{ij}$  depends on the angles  $\theta_i$ ,  $\theta_j$  and  $\phi_{ij}$ , describing the relative orientation of the electronic transition dipole moments  $\mu_{S_1 \leftarrow S_0}$  shown Fig. 20A.

$$\kappa_{ij} = \sin \theta_i \sin \theta_j \cos \phi_{ij} - 2 \cos \theta_i \cos \theta_j \quad (36)$$

Energy transfer between donors and acceptors consisting of different molecules must be distinguished from energy migration which takes place between alike molecules.

We consider a zeolite L crystal which contains alike dye molecules, large enough so that orbital overlap is not possible. This imposes restrictions on the angles between the electronic transition moments we must consider, see Fig. 20. The two important situations where the electronic transition moments of the molecules are strictly oriented parallel to the channel axis and random orientation have been studied quantitatively in ref. [75]. Here we consider the angles  $\theta - \alpha_{ij}$  and  $\pi - \theta + \alpha_{ij}$  which are equally probable.  $\theta$  is the angle between the transition moments and the crystal axis. This means that  $\kappa_{ij}^2$  can be expressed as follows:

$$\kappa_{ij}^2 = \left[ (\sin^2(\theta - \alpha_{ij}) \cos \phi_{ij} - 2 \cos^2(\theta - \alpha_{ij})) \right]^2 \quad (37)$$

The angle  $\alpha_{ij}$  is the angle between the site where the excited molecule  $j$  is located and any other site  $i$ . It can be expressed as

$$\alpha_{ij} = \arccos\left(\frac{z_{ij}}{R_{ij}}\right) \quad (38)$$

where  $R_{ij}$  and  $z_{ij}$  are given by eqs. (9) and (11). Averaging over all  $\phi_{ij}$  leads to:

$$\kappa_{ij}^2 = \frac{9}{2} \cos^4(\theta - \alpha_{ij}) - \cos^2(\theta - \alpha_{ij}) + \frac{1}{2} \quad (39)$$

The averaging takes into account that each channel is surrounded by six other channels.

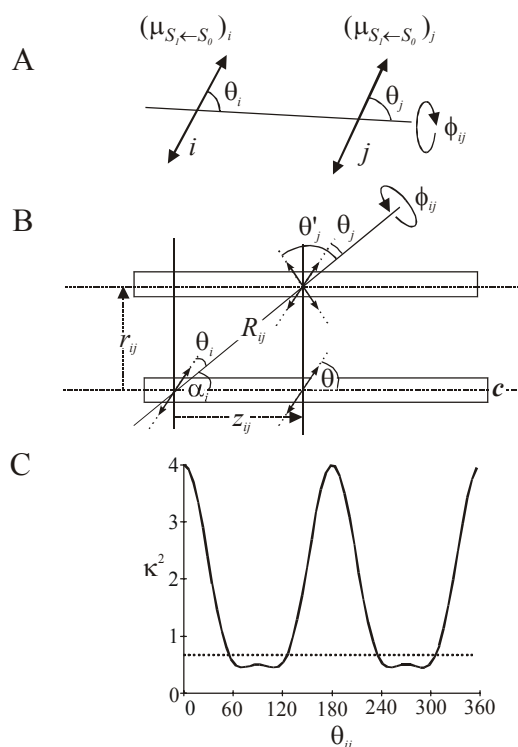


**Figure 20.** (A) Angles  $\theta_i$ ,  $\theta_j$  and  $\phi_{ij}$ , describing the relative orientation of the electronic transition dipole moments  $\mu_{S_1 \leftarrow S_0}$  between two dye molecules. (B) Relative orientations of the electronic transition dipole moments between two equal dye molecules in the channels of zeolite L. (C) Angular dependence of the orientation factor  $\kappa^2$  under the anisotropic conditions (B) and averaged over  $\phi_{ij}$ .

Arrangements of densely packed non overlapping dye molecules are illustrated in Fig. 21A. The molecule in the middle is in its first excited electronic state. It can relax to the ground state either by emitting a photon or by transferring its excitation energy to a molecule in the surrounding. We do not impose any restrictions on the angle  $\phi_{ij}$ , despite of the fact that some preferences are to be expected in a hexagonal crystal. Averaging as expressed in eq. (39) is valid unless crystals containing only very few molecules are investigated. It is interesting to realize that a similarly simple situation can exist for energy transfer between different kinds of molecules, provided they are of similar shape. This situation is shown in Fig. 21B. The donor in the middle is in its first electronic excited state. It can either relax to

the ground state by emitting a photon or by transferring the excitation energy to a different kind of molecule. This situation can experimentally be realized e.g. by using  $\text{Py}^+$  (donor) and  $\text{Ox}^+$  (acceptor). Energy migration between alike molecules is another competing process.

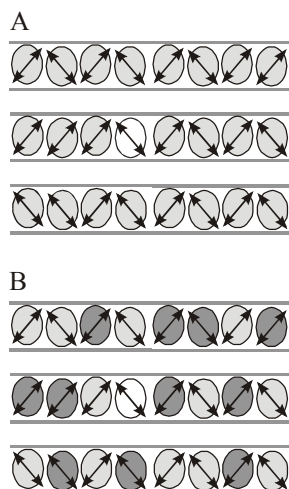


**Figure 21.** (A) Densely packed alike molecules. The white molecule in the middle is in its first electronic excited state. (B) Densely packed donor (darker) and acceptor (lighter) molecules which have the same shape. The white donor in the middle is in its first electronic excited state.

We consider a crystal which contains donor molecules in its body and a thin layer of traps at both ends, as illustrated in Fig. 1. Another way to explain this material is shown in Fig. 22. Somewhere in the bulk a donor is electronically excited by absorbing a photon. We are interested in knowing how fast the excitation energy migrates in the crystal depending on the occupation probability and the characteristics of the dye. We would also like to know how the front back trapping efficiency depends on these characteristics and on the size of the crystal and we would like to understand the luminescence decay of the donors and of the traps.

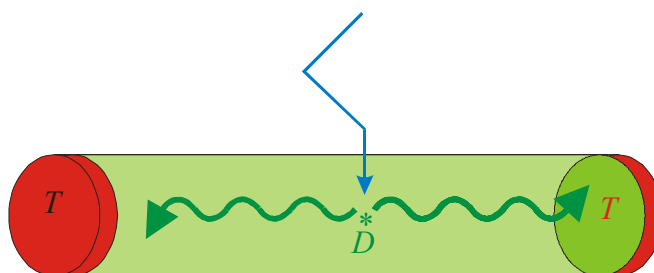


**Figure 22.** Representation of a cylindrical host containing non-interacting donor molecules  $D$  and at both ends a layer of traps  $T$ .

We do not know which donor  $D$  has been excited. We therefore assume that immediately after irradiation at  $t = 0$  all sites  $i$  have the same excitation probability  $P_i(0)$ , while all traps  $T$  are in the ground state, hence  $P_T(0) = 0$ . These probabilities change with time because of energy migration, relaxation processes, and trapping. The excitation probability  $P_i(t)$  is governed by the following master equation:



$$\frac{dP_i(t)}{dt} = \sum_j P_j(t)k_{ji}^{EM} - P_i(t)k_i \quad (40)$$

The sites  $i$  are populated by energy migration starting from any other site  $j$  with the corresponding rate constants  $k_{ji}^{EM}$ . They are depopulated by spontaneous emission, by radiationless decay, by energy migration to all sites  $j \neq i$  and by energy transfer to trapping sites  $J$ . The depopulation rate of an excited donor  $i$  is given by:

$$k_i = k_D^F + k_D^{rd} + k_i^{EM} + k_i^{ET} \quad (41)$$

where  $k_D^F$  is the intrinsic fluorescence rate constant of the donor and  $k_D^{rd}$  is the rate constant of thermal relaxation of the donor including internal conversion and intersystem crossing. The energy migration rate constant  $k_i^{EM}$  is obtained by summing up all the individual  $k_{ij}^{EM}$  for the energy migration between an excited donor  $i$  and surrounding acceptors  $j$ :

$$k_i^{EM} = \sum_{i \neq j} k_{ij}^{EM} \quad (42)$$

The energy transfer rate constant  $k_i^{ET}$  can be obtained similarly:

$$k_i^{ET} = \sum_J k_{iJ}^{ET} \quad (43)$$

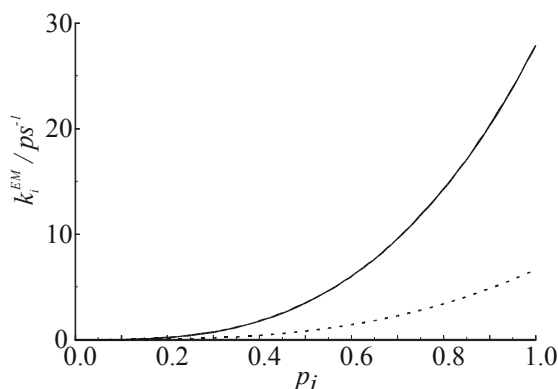


**Figure 23.** Energy migration rate constant  $k_i^{EM}$  as a function of the occupation probability  $p_i$  for two spectral overlaps (solid:  $4.40 \cdot 10^{-13} \text{ cm}^3 \text{ M}^{-1}$  and dashed:  $1.05 \cdot 10^{-13} \text{ cm}^3 \text{ M}^{-1}$ ).

The traps are a sink for the electronic excitations of the donors. The donors are considered as the only source for electronic excitation of the traps. The traps,  $T$ , can relax by emitting a photon with a rate constant  $k_T^F$  or by thermal relaxation  $k_T^{rd}$ . This can be expressed as follows:

$$\frac{dP_J(t)}{dt} = \sum_i k_{iJ}^{ET} P_i(t) - (k_T^F + k_T^{rd}) P_J(t) \quad (44)$$

Thus, the time evolution of the excitation probabilities  $P_i(t)$  and  $P_j(t)$  is described by eqs. 40 and 44. This allows us to write for time  $t+\Delta t$ :

$$P_i(t + \Delta t) = P_i(t) + \frac{dP_i(t)}{dt} \Delta t \quad (45)$$

$\Delta t$  is considered to be small enough so that higher order terms can be neglected. Combining eqs. (40) and (45) leads to the following homogeneous Markoff chain:

$$P_i(t + \Delta t) = P_i(t)(1 - k_i \Delta t) + \sum_j P_j(t) k_{ji}^{EM} \cdot \Delta t \quad (46)$$

The Markoff chain which describes the total trapping  $P_J^0$  can be expressed analogously.

$$P_J^0(t + \Delta t) = P_J^0(t) + \sum_i P_i(t) k_{iJ}^{ET} \Delta t \quad (47)$$

If the fate of the trapped quanta is taken into account, this equation becomes:

$$P_J(t + \Delta t) = P_J(t)(1 - (k_T^F + k_T^d) \Delta t) + \sum_i P_i(t) k_{iJ}^{ET} \Delta t \quad (48)$$

where  $P_J$  describes the excitation probability of the traps. The probability that the electronic excitation has reached a trap during the whole time period  $t$  after excitation is the trapping probability  $P_T(t)$  [75]. It is the sum of the trapping  $P_J^0$  of all trapping sites  $J$  up to this time.

$$P_T(t) = \sum_J P_J^0(t) \quad (49)$$

The trapping rate  $dP_T/dt$  is given by the sum of energy transfer rates from any site donor  $i$  to any trap site  $J$ .

$$\frac{dP_T(t)}{dt} = \sum_i \sum_J P_i(t) k_{iJ}^{ET} \quad (50)$$

The trapping efficiency  $P_T(\infty)$  is equal to the sum of the excitation probabilities of all trapping sites  $J$  at infinite time after irradiation.

$$P_T(\infty) = \lim_{t \rightarrow \infty} P_T(t) = \lim_{t \rightarrow \infty} \sum_J P_J^0(t) \quad (51)$$

The fluorescence rates of the donors and the traps are given by:

$$v_D^F(t) = - \sum_i P_i(t) k_D^F \quad (52)$$

$$v_T^F(t) = - \sum_J P_J(t) k_T^F \quad (53)$$

The average fluorescence rate constants  $k_D^F$  and  $k_T^F$  are assumed to be the same for all donors and traps, respectively. The integrated fluorescence  $FD(t)$  and  $FT(t)$  are equal to the probability that the electronic excitation has left the system by donor and trap fluorescence, respectively, at time  $t$  after irradiation.  $FD(t)$  is thus equal to the probability that electronic excitation is neither on a site  $i$  nor on a site  $J$ .

$$FD(t) = 1 - \sum_i P_i(t) - \sum_J P_J(t) \quad (54)$$

Using the same arguments for  $FT(t)$  we can write:

$$FT(t) = \sum_J P_J(t) \quad (55)$$

We have distinguished between *front trapping*, which refers to traps positioned only on the front side of the cylindrical microcrystals, *front-back trapping*, which refers to traps on the front and to traps on the back positioned in the slab, *coat trapping*, which refers to traps positioned on the coat of the cylinder, *axial trapping*, which refers to traps located in the central channel, and *point trapping*, which refers to a single trap positioned at the center of the front side [75]. All these trapping types reflect symmetry aspects of the cylinder investigated. Here we concentrate on front-back trapping  $T_{FB}(t)$ , because it is the case for which the best experimental data are available, so far.

*Front-back and front trapping:* A slab on both sides of the crystal is reserved for traps, as explained in Figs. 1 and 22. Calculation of these trapping types requires knowledge of the excitation distribution  $Pz$  along  $c$ . The excitation distribution  $Pz$  describes the excitation probabilities  $P_m(t)$  of whole slabs  $m$ .  $P_m(t)$  is equal to the sum of the occupation probabilities of all sites  $i$  belonging to slab  $m$ . The time evolution of  $P_m(t)$  is based on energy migration along  $c$ . The energy transfer rate constant  $k_{zm}$  from slab  $m$  to slab  $n$  is assumed to be equal to the sum of the rate constants for energy transfer starting from site  $(0,0)$  in slab  $m$  to any other site  $(n_a, n_b)$  in slab  $n$ .

$$k_{zm} = \sum_{\text{all } (n_a, n_b) \text{ pairs}} k_{mn}(z_{mn}, y(n_a, n_b)) \quad (56)$$

The rate constant  $k_{z_{mN}}$  for energy transfer from slab  $m$  to a trap containing slab  $N$  is calculated analogously, but based on the rate constants  $k_{mN}$ . The time evolution of  $Pz_m(t)$  and  $Pz_N(t)$  are calculated according to eqs. (46) and (47), respectively.

$$Pz_m(t + \Delta t) = Pz_m(t) \left( 1 - \sum_n k_{zm} \Delta t \right) + \sum_n Pz_n(t) k_{zn} \Delta t \quad (57)$$

$$Pz_N^0(t + \Delta t) = Pz_N^0(t) + \sum_m Pz_m^0(t) k_{z_{mN}} \Delta t \quad (58)$$

$$Pz_N(t + \Delta t) = Pz_N(t) (1 - (k_T^F + k_T^d) \Delta t) + \sum_m Pz_m(t) k_{z_{mN}} \Delta t \quad (59)$$

$Pz_m(t)$  and  $Pz_N(t)$  express the excitation distribution among the slabs. For front-back trapping, traps are found in the first and the last slab, which we call slabs 0 and  $m_{max}$ .  $T_S^{FB}(t)$  is therefore equal to the sum of the excitation probabilities in both slabs at time  $t$ .

$$T_S^{FB}(t) = Pz_0^0(t) + Pz_{m^{max}}^0(t) \quad (60)$$

The competition between the trapping and the fluorescence of the donors can be calculated as explained in ref. [75].

We illustrate in Fig. 24A the influence of trapping and spontaneous emission of the donors on the excitation distribution  $Pz(m,t)$  for a row of 90 slabs where the first and the last ones are occupied by traps. Immediately after excitation all slabs have the same excitation probability.  $Pz(m,t)$  is shown after 5, 10, 50, and 100 ps. We observe that the slabs close to the acceptor layers very quickly lose their excitation energy. The trapping rate is proportional to the gradient of  $Pz(m,t)$  at the position of the traps. Hence, it depends not only on the remaining excitation probability but also on the excitation distribution. This in contrast to the donor fluorescence rate, which depends only on the excitation distribution of the donors, eq. 52. The fluorescence rate of the traps is proportional to their excitation probability, eq. 53. We therefore expect a fluorescence decay behavior as illustrated in Fig. 24B. The fluorescence decay of the donors becomes much faster in presence of traps, because of the depopulation due to the irreversible energy transfer to the traps. The fluorescence intensity stemming from the traps initially increases because excited states must first be populated via energy transfer from the donors. It therefore goes through a maximum.

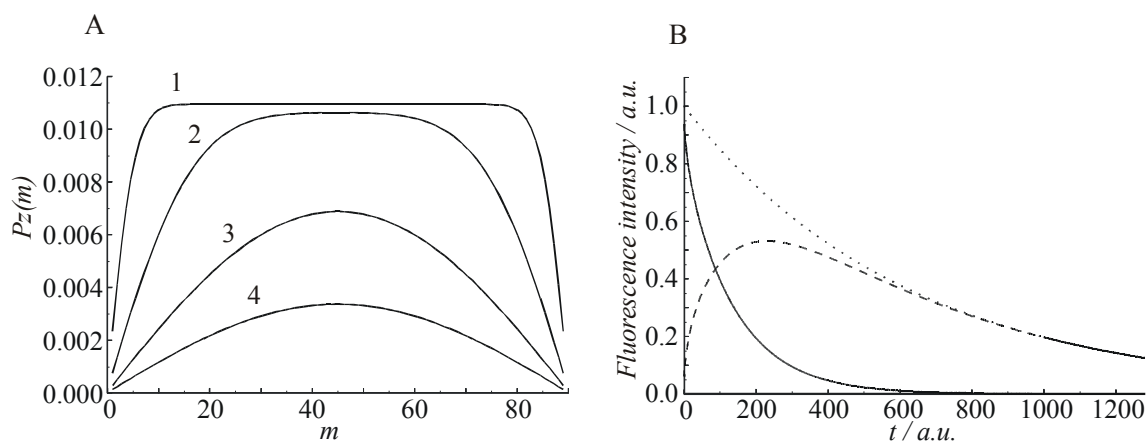


**Figure 24.** (A) Excitation distribution along the channel axis of a zeolite L crystal consisting of 90 slabs under the condition of equal excitation probability at  $t = 0$  calculated for front-back trapping. Fluorescence of the donors is assumed. **1:**  $t = 5$  ps, **2:**  $t = 10$  ps, **3:**  $t = 50$  ps, and **4:**  $t = 100$  ps after irradiation. (B) Luminescence decay of the donors in absence of traps (dotted), in presence of traps at both ends (solid), and luminescence decay of the acceptors (dashed).

### C. Spectral Overlap

The spectral overlap  $J_{ij}$  is an important quantity in radiationless energy transfer and migration, as we have seen in eq. 32. It is equal to the integral of the corrected and normalized fluorescence intensity  $I_i^F(\bar{\nu})$  of the donor multiplied by the extinction coefficient  $\varepsilon_j(\bar{\nu})$  of the acceptor as a function of the wave number  $\bar{\nu}$ , and it is usually expressed in units of  $\text{cm}^3\text{M}^{-1}$ .

$$J_{ij} = \int_0^{\infty} \varepsilon_j(\bar{\nu}) I_i^F(\bar{\nu}) \frac{d\bar{\nu}}{\bar{\nu}^4} \quad (61)$$

The meaning of the spectral overlap is best understood by considering the spectra of the donor ( $\text{Py}^+$ ), acceptor ( $\text{Ox}^+$ ) pair illustrated in Fig. 25.

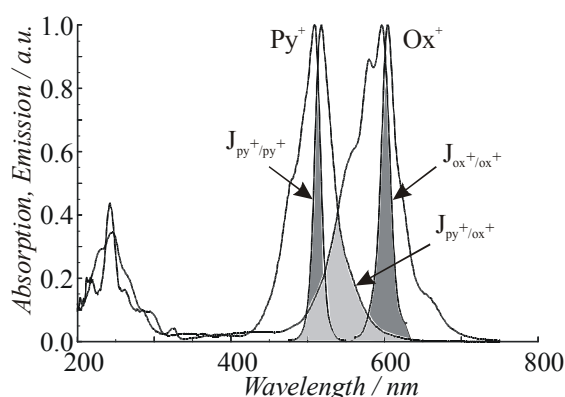


**Figure 25.** Absorption (solid) and fluorescence (dashed) spectra of  $\text{Py}^+$  and  $\text{Ox}^+$  in zeolite L, measured in an aqueous dispersion. The different spectral overlap regions are shaded.

It is difficult to measure the oscillator strengths of molecules embedded in a matrix. Despite of this, good values of  $J_{ij}$  can be determined as a function of the temperature. A procedure we have used to extract the information from excitation spectra was to set the maximum of the excitation spectrum measured at room temperature equal to the extinction coefficient at the absorption maximum in solution. The integrals of the excitation spectra were then normalized to the integral of the corresponding spectrum at room temperature. This is reasonable because the oscillator strength  $f$  of a transition  $n \leftarrow m$  does not depend on the temperature.

$$f = \frac{8\pi^2 \bar{\nu} c m_e}{3 h e^2} \left| \vec{\mu}_{nm}^{ed} \right|^2 \quad (62)$$

where  $c$  is the speed of light,  $m_e$  is the mass of an electron,  $h$  is Planck's constant, and  $e$  is the elementary charge. The electronic transition-dipole moment  $\vec{\mu}_{nm}^{ed}$  between two wave functions  $\psi_n$  and  $\psi_m$  is defined as

$$\vec{\mu}_{nm}^{ed} = \langle \psi_n | \vec{\mu}_{ed} | \psi_m \rangle \quad (63)$$

The oscillator strength is a temperature independent intrinsic property of a molecule. The relation between the molar decadic extinction coefficient  $\varepsilon$  and the oscillator strength  $f$  can be expressed as follows [76]:

$$f = 4.32 \cdot 10^{-9} \int_{band} \varepsilon(\bar{\nu}) d\bar{\nu} \quad (64)$$

A general way to predict the temperature dependence of the spectral overlap is not known. We found that  $J_{Py^+/Py^+}$ ,  $J_{Ox^+/Ox^+}$  and also  $J_{Py^+/Ox^+}$  do not change significantly in the temperature range from 80 K to 300 K, see Fig. 26. The large difference between the absolute values of the overlap integrals  $J_{Py^+/Py^+}$ ,  $J_{Ox^+/Ox^+}$  is due to a different Stokes shift ( $140 \text{ cm}^{-1}$  for  $Ox^+$ ,  $560 \text{ cm}^{-1}$  for  $Py^+$ ). Other cases which show a temperature dependence of the spectral overlap also exist [3].

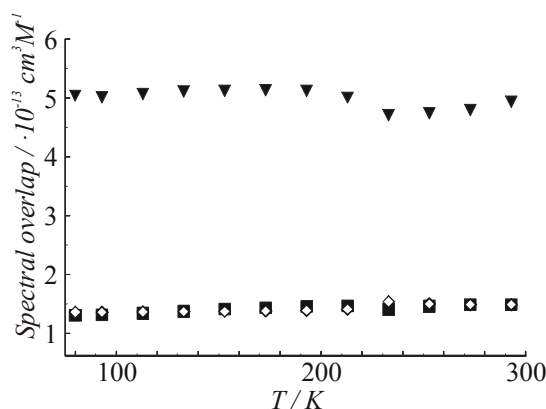


**Figure 26.** Temperature dependence of the spectral overlap of  $Py^+/Py^+$  (■),  $Ox^+/Ox^+$  (▼), and  $Py^+/Ox^+$  (◇) in zeolite L, measured on thin layers coated on quartz plates.

#### IV. ELEGANT EXPERIMENTS FOR VISUAL PROOF OF ENERGY TRANSFER AND MIGRATION

Photonic antenna properties of supramolecularly organized dye molecules for light harvesting, transport, and trapping depend critically on their ability to support fast radiationless energy migration and transfer. We present in this chapter three experiments which beautifully illustrate the exciting capabilities of the dye zeolite material for this purpose. We start with an experiment which we have used many times for classroom demonstration of Förster energy transfer. The second experiment provides a simple tool to investigate intracrystalline transport of dyes by observing energy transfer from a donor to an acceptor molecule. Very efficient and easily detectable energy migration is illustrated in the third experiment where data of  $Py^+$  loaded and  $Ox^+$  modified zeolites of different lengths are shown.

## A. Energy transfer

The visual proof of energy transfer in this experiment is based on the observation that  $\text{Py}^+$  and  $\text{Ox}^+$  are incorporated into zeolite L from an aqueous solution with about equal rates. It is therefore possible to control the mean distance between donors  $D$  and acceptors  $A$  by varying the occupation probability. The main processes are energy transfer and luminescence as illustrated in Fig. 27. Energy migration between the donor molecules and between the acceptor molecules, which are of similar probability as the energy transfer, and also radiationless relaxation processes are not indicated.

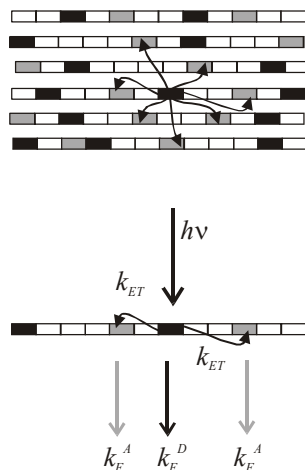


**Figure 27.** Scheme of a few channels of a zeolite L crystal containing acceptor  $A$  (gray rectangles) and donor  $D$  (black rectangles) molecules. Each rectangle marks a site. The main processes taking place after excitation of a donor are indicated in the lower part.  $k_{ET}$  is the rate constant for energy transfer.  $k_F^A$  and  $k_F^D$  are the rate constants for fluorescence.

The seven luminescent samples shown in Fig. 28 consist of zeolite L crystals of 300 nm average length filled with different amounts of  $\text{Py}^+$  (donor  $D$ ) and  $\text{Ox}^+$  (acceptor  $A$ ). In all cases  $\text{Py}^+$  was specifically excited at  $485 \pm 5$  nm, where the absorption of  $\text{Py}^+$  is strong and that of  $\text{Ox}^+$  very weak as can be seen from the samples **1** and **7** which are the references. **1** is loaded with  $1.25 \cdot 10^{-3}$  M  $\text{Py}^+$  and **7** is loaded with the same amount of  $\text{Ox}^+$ . The other samples contain a 1:1 mixture of  $\text{Py}^+$  and  $\text{Ox}^+$  of the following concentrations: **2**,  $2.50 \cdot 10^{-4}$  M; **3**,  $1.25 \cdot 10^{-3}$  M; **4**,  $2.50 \cdot 10^{-3}$  M; **5**,  $5.00 \cdot 10^{-3}$  M; **6**,  $1.00 \cdot 10^{-2}$  M. A rough estimate of the mean donor to acceptor distance  $R_{DA}$  can be obtained by assuming isotropic conditions and equal concentrations of donor and acceptor:

$$R_{DA} = \left[ \frac{3}{4\pi} \frac{1}{c_A N_A} \right]^{1/3} \quad (65)$$

$N_A$  is the Avogadro number and  $c_A$  is the concentration of  $\text{Ox}^+$  in the zeolite nanocrystal. From this we obtain the following mean donor-acceptor distances: **2**, 96 Å; **3**, 68 Å; **4**, 54 Å; **5**, 43 Å; **6**, 34 Å. The Förster radius for  $\text{Py}^+$  to  $\text{Ox}^+$  energy transfer in a medium of refractive index of 1.4 is about 70 Å, based on the  $\text{Py}^+/\text{Ox}^+$  spectral overlap which is  $1.5 \cdot 10^{-13} \text{ cm}^3 \text{ M}^{-1}$ . We observe in **2** mainly the green luminescence of  $\text{Py}^+$ , this means that energy transfer is unimportant. But the yellow color of **3** is due to a mixture of green and red luminescence which means that energy transfer is significant in this sample. It becomes more and more

important with increasing concentration so that at the end, sample **6**, the red luminescence stemming from excited  $Ox^+$  is dominant.



**Figure 28.** Photographic picture of the fluorescence of dye loaded zeolite L layers upon monochromatic irradiation at  $485\pm 5$  nm and observation through a 500 nm cutoff filter. **1** and **7** are references loaded with  $Py^+$  and  $Ox^+$  only. **2** to **6** contain a 1:1 mixture of  $Py^+$  and  $Ox^+$  of the following concentrations: **2**,  $2.50\cdot 10^{-4}$  M; **3**,  $1.25\cdot 10^{-3}$  M; **4**,  $2.50\cdot 10^{-3}$  M; **5**,  $5.00\cdot 10^{-3}$  M; **6**,  $1.00\cdot 10^{-2}$  M.

The same experiment can be carried out quantitatively. Taking into account radiationless processes, namely internal conversion  $k_{IC}$  intersystem crossing  $k_{ISC}$  and bimolecular quenching  $k_Q[Q]$  with a quencher  $Q$ , the time dependent concentrations of the donor  $D$  and the acceptor  $A$  in the excited singlet state  $S_1$ ,  $[D_{S_1}]$  and  $[A_{S_1}]$  can be expressed as follows:

$$\frac{d[D_{S_1}]}{dt} = j_{abs} - (k_{ET} + k_F^D + k_{IC}^D + k_{ISC}^D + k_Q^D[Q])[D_{S_1}] = j_{abs} - [D_{S_1}] \sum k_d^D \quad (66)$$

$$\frac{d[A_{S_1}]}{dt} = k_{ET}[D_{S_1}] - (k_F^A + k_{IC}^A + k_{ISC}^A + k_Q^A[Q])[A_{S_1}] = k_{ET}[D_{S_1}] - [A_{S_1}] \sum k_d^A \quad (67)$$

where  $j_{abs}$  is the number of photons absorbed per unit time. The fluorescence quantum yield of the donor  $\Phi_F^D$  and of the acceptor  $\Phi_F^A$  under stationary conditions is therefore:

$$\Phi_F^D = \frac{k_F^D}{\sum k_d^D} \quad (68)$$

$$\Phi_F^A = \frac{k_{ET}}{\sum k_d^D} \frac{k_F^A}{\sum k_d^A} \quad (69)$$

A quantity which in many cases can easily be measured, even in a heterogeneous system, is the ratio between these two fluorescence quantum yields. We therefore write:

$$\frac{\Phi_F^A}{\Phi_F^D} = k_{ET} \frac{k_F^A}{k_F^D} \frac{1}{\sum k_d^A} \quad (70)$$



This equation shows that the ratio between the acceptor and donor fluorescence quantum yields is directly proportional to the energy transfer rate constant  $k_{ET}$ . We have shown that this leads to the following linear relation between the fluorescence intensity of the acceptor  $I_{Ox}$  and that of the donor  $I_{Py}$ , and the occupation probability  $p_{Ox}$  of the acceptor [3, 77]:

$$\frac{I_{Ox}}{I_{Py}} = Cp_{Ox} \quad (71)$$

where  $C$  is a constant. We show in Fig. 29 the luminescence spectra measured in an aqueous suspension of similar materials as **2** to **6** in Fig. 28. Aqueous suspensions were chosen because this is the easiest way for quantitative measurements. We observe that the acceptor emission is unimportant at low loading and that it becomes dominant at high loading. We also observe that the linear relation between the ratio of the acceptor to donor luminescence intensity and the acceptor loading (71) is well fulfilled, with a constant  $C = 121$  sites.

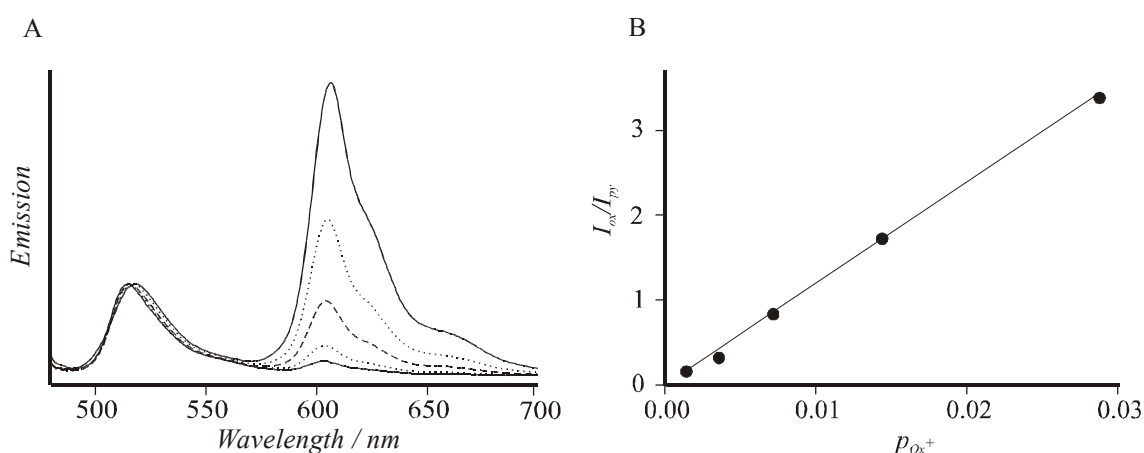


**Figure 29.** Fluorescence of 5 suspensions with  $p_{Ox^+} = 0.0014, 0.0036, 0.0072, 0.0144$  and  $0.0288$  after specific excitation of  $Py^+$  at  $465$  nm for equal  $p_{Ox^+}$  and  $p_{Py^+}$ . (A) Fluorescence spectra normalized to the same peak height for the  $Py^+$  emission at about  $520$  nm. The intensity of the oxonine emission (peak on the right) increases with increasing  $p$ . (B) Ratio of the fluorescence intensity  $I_{Ox}$  of  $Ox^+$  and  $I_{Py}$  of  $Py^+$  as a function of the loading.

## B. Intrazeolite diffusion monitored by energy transfer

The energy transfer between donors  $Py^+$  and acceptors  $Ox^+$  can be used for observing the linear diffusion kinetics of these dyes inside the zeolite L channels. We assume that in all channels a situation can be prepared as illustrated in Fig. 30, at the beginning of the experiment. Immediately after all dye molecules have entered the zeolite channels, the maximum energy transfer is observed because the donor to acceptor distance is short. The donor to acceptor distance increases, and hence the energy transfer rate decreases, when the molecules diffuse deeper into the channels. From this the following relation for diffusion kinetics is found under the condition that the initial distributions of the donors and the acceptors are the same,  $p_{Py^+}^0 \approx p_{Ox^+}^0$ , denoted as  $p^0$ . Experimental details can be found in [77].

$$\frac{I_{Ox^+}}{I_{Py^+}}(t) = C \frac{(p^0)^2}{\sqrt{8\pi}} \frac{1}{\sqrt{D_0 t}} \quad (72)$$

where  $C$  is the same constant as in eq. 71,  $t$  is the time and  $D_0$  the dye diffusion coefficient. This means that the ratio of the acceptor to donor fluorescence intensities is proportional to the inverse square root of time.

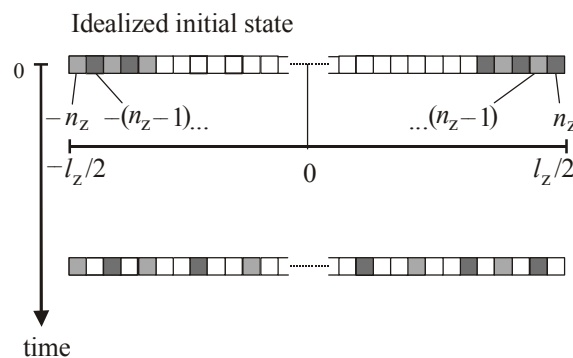


**Figure 30.** Diffusion of dye molecules in the channels of zeolite L. Idealized initial state of a channel and state after diffusion has occurred for some time.

Several experimental conditions must be realized for the application of eq. 72. The donor and acceptor molecules should enter the channels at about the same rate, so that the assumptions made for the initial state are sufficiently well fulfilled. They should not be able to glide past each other once they are inside the channels. The crystals should be so long that molecules entering from both sides do not reach each other in the middle part of the channels during the time of observation. These conditions can be fulfilled for the donor/acceptor pair  $Py^+/Ox^+$  in zeolite L. Moreover, different stages of the diffusion can be observed by means of an optical microscope.

We show in Fig. 31, fluorescence microscopy images of a sample after 20 min, 60 min, 470 min, and 162 h reaction time at 88°C. The images were obtained by specifically exciting  $Py^+$  at 470 - 490 nm with the exception of **3b** where  $Ox^+$  was excited at 545 - 580 nm. Two selected crystals are framed, to represent what we observed for most crystals. When comparing the images **1**, **2**, **3a**, and **4** (increasing reaction times), we first notice the progress of the insertion (**1** → **2**) of the dye molecules and then their diffusion inside the zeolite channels, by considering both the size and the color of the fluorescent spots. The fluorescence of  $Py^+$  appears green and that of  $Ox^+$  deep red, while yellow colors are due to mixtures of red and green. Since specifically  $Py^+$  was excited, the red contribution is due to energy transfer from the excited  $Py^+$  to  $Ox^+$ . We observe two yellow-red spots on both sides of the crystals in image **1**. In image **2** the spots have extended and, in the middle part, a weak green region appears. While it is hardly visible in **2**, it becomes obvious in **3a**. If  $Ox^+$  is excited specifically, as illustrated in **3b**, its presence in the inner region of the channel can be seen. This also shows that the mean distance between the donor and acceptor molecules is greater in the middle than at the ends of the channels. The green color dominates after the very long reaction time and extends over the whole crystal, as in **4**. The intensity distribution shows that the equilibrium has not yet been reached. Red fluorescence of the same shape is observed if specifically  $Ox^+$  is excited. This means that the distribution of  $Py^+$  and  $Ox^+$  in the crystals is the same or at least similar. The images in Fig. 31 support the assumptions made, that  $Py^+$  and  $Ox^+$  enter the channel of zeolite L at about the same rate.

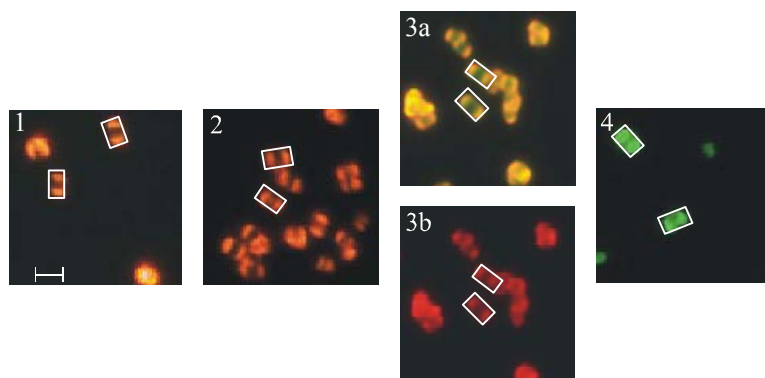


**Figure 31.** Fluorescence microscopy pictures to visualize the diffusion of  $\text{Ox}^+$  to  $\text{Py}^+$  in zeolite L. The images were taken after **1** 20 min, **2** 60 min, **3** 470 min, and **4** 162 h, respectively. They were obtained by exciting  $\text{Py}^+$  at 470-490 nm, with the exception of **3b** where  $\text{Ox}^+$  was specifically excited at 545-580 nm. Two crystals of each image are framed. The scale given in **1** corresponds to a length of  $1.5 \mu\text{m}$  ( $p_{\text{Py}^+} = p_{\text{Ox}^+} = 0.008$ ).

### C. Energy migration

We now show an experiment which illustrates how the photonic antenna principle of Fig. 1 can be realized. Again  $\text{Py}^+$  and  $\text{Ox}^+$  were found to be very convenient dyes for this purpose. The channels of zeolite L are first loaded with  $\text{Py}^+$  and then modified at both sides with  $\text{Ox}^+$ . The latter acts as a luminescent trap which gets excited via radiationless energy transfer from an excited  $\text{Py}^+$ . If radiationless relaxation is not considered,  $\text{Ox}^+$  can lose its energy only by fluorescence, as it cannot transfer it back to  $\text{Py}^+$  because of its lower excitation energy. Fluorescence of excited  $\text{Py}^+$ , internal conversion, and intersystem crossing compete with the energy migration and energy transfer. The arrangement shown allows to investigate the efficiency of energy migration among the  $\text{Py}^+$  molecules along the crystals as a function of its lengths. We show in Fig. 32 the images of some large zeolite L crystals loaded with  $\text{Py}^+$  and modified with  $\text{Ox}^+$  upon specific excitation of  $\text{Py}^+$  at 470-490 nm. Two separate regions of fluorescence can be distinguished. We recall that the resolution of the optical microscope is in the order of half the emitted wavelength. The middle region of the crystals fluoresces green because of the  $\text{Py}^+$ . The emission at both ends of the crystals appears yellowish due to the mixing of the green  $\text{Py}^+$  and the red  $\text{Ox}^+$  emission.  $\text{Ox}^+$  is not excited directly but via energy transfer from  $\text{Py}^+$ .

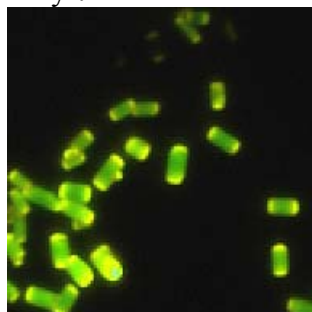


**Figure 32.** True color microscope pictures of  $\text{Py}^+$  loaded and  $\text{Ox}^+$  modified zeolite L crystals of about 2400 nm length, after excitation of only  $\text{Py}^+$  at 470-490 nm.

We expect that the trapping efficiency increases with decreasing crystal length  $l_z$  for otherwise constant parameters, specifically constant  $p_{\text{Py}^+}$ , because the excitation energy has to migrate over an increasingly large distance to reach a trap. This can be tested if materials with different average crystal lengths are available over a significant range. Since we have been able to prepare these materials, experiments with crystals of the following average length were carried out: **1**, 300 nm; **2**, 500 nm; **3**, 850 nm; **4**, 1400 nm; and **5**, 2400 nm. These crystals were loaded with  $\text{Py}^+$  so that the occupation probability was always the same, namely  $p_{\text{Py}^+} = 0.11$ . They were then modified with two  $\text{Ox}^+$  molecules on average at both ends of the channels. The fluorescence of a thin layer on quartz was measured at room temperature after specific excitation of  $\text{Py}^+$  at 460 nm. The fluorescence reported in Fig. 34 is scaled to the same height at the  $\text{Py}^+$  emission maximum, as before. Fig. 33 shows a very strong increase of the  $\text{Ox}^+$  emission with decreasing crystal length  $l_z$ . One can calculate that the front-back trapping efficiency increases from 0.33 up to 0.91. This means that in the 300 nm crystals, 90% of the emitted light is due to energy migration along the  $\text{Py}^+$  and transfer to the luminescent traps  $\text{Ox}^+$ . Interestingly, in these experiments carried out at constant  $\text{Py}^+$  loading, there is also a small shift of the  $\text{Py}^+$  maximum, from 525 nm for the smallest crystals to 530 nm for the largest ones. The maximum of the  $\text{Ox}^+$  emission remains at 605 nm. This wavelength shift is most probably due to self-absorption and re-emission because the absorption depth increases with increasing crystal size despite of the constant  $p_{\text{Py}^+}$  [53]. The measurements were made on thin dye-loaded zeolite L layers on quartz plates. The pronounced increasing trapping efficiency with decreasing length of the zeolite L underlines the interpretation that the antenna behavior is mainly governed by Förster type energy transfer, supported by some self-absorption and re-emission. The latter causes a shift in the maximum of the  $\text{Py}^+$  fluorescence spectrum with increasing loading, but also with increasing crystal size at constant loading [3]. Some internal reflection may also occur, especially in the larger crystals, where it increases the absorption probability.

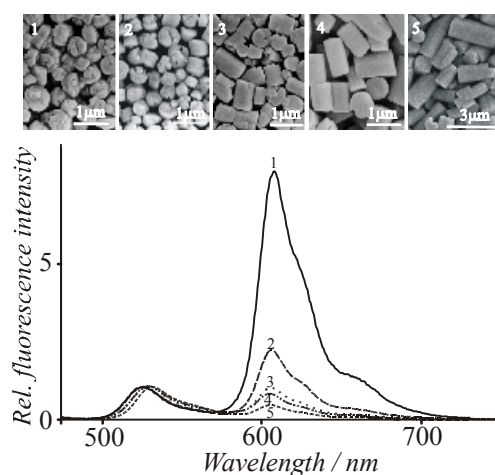


**Figure 33.** *Upper:* EM pictures of the investigated zeolite L samples with different crystal length  $l_z$ : **1**, 300 nm; **2**, 500 nm; **3**, 850 nm; **4**, 1400 nm; **5**, 2400 nm. *Lower:* Fluorescence intensity after specific excitation of only  $\text{Py}^+$  at 460 nm (scaled to the same height at the maximum of the  $\text{Py}^+$  emission) of  $\text{Py}^+$  loaded and  $\text{Ox}^+$  modified zeolite L crystals with constant  $\text{Py}^+$  loading ( $p_{\text{Py}^+} = 0.11$ ) as a function of crystal length. The  $\text{Ox}^+$  modification was two molecule at both ends of the channel, on average.

## V. CONCLUSIONS

This work shows that zeolite L is a very suitable framework for the arrangement of a wide variety of chromophores. The structure of zeolite L is such that the formation of non-fluorescent dimers inside the channels can be prohibited and chromophores can be aligned in a certain direction. We have shown that this host/guest system can be used to make very efficient nanoscale two-directional photonic antenna systems. A broad spectral absorption range can be achieved by using several different cationic and neutral dyes.

It is a challenge to couple the antenna systems to a device, e.g. a semiconductor. It has already been shown that it is possible to prepare organized zeolite monolayers on flat surfaces [78, 79]. For coupling, the interface between the chromophore loaded zeolite L antenna systems and the semiconductor becomes very important. Stopcock molecules are expected to function as a bridge between the chromophores in the zeolite L channels and the device surface. This will open a whole new exciting research area.

## ACKNOWLEDGMENTS

This work was supported by the Swiss National Science Foundation Project NFP 47 (4047-057481), project NF 2000-053414/98/1 and by the Bundesamt für Energie, Project 10441. We also thank René Bühler for his many helps when carrying out the experiments and preparing the figures. We thank Cindy Hendrikx for measuring and preparing Fig. 10, and Stephan Glaus for Fig. 4.

## REFERENCES

- [1] R. F. Cracknell, K. E. Gubbins, M. Maddox, D. Nicholson, *Acc. Chem. Res.*, **28**, 281 (1995).
- [2] J. M. Thomas, *Angew. Chem.*, **111**, 3800 (1999).
- [3] G. Calzaferri, D. Brühwiler, S. Megelski, M. Pfenniger, M. Pauchard, B. Hennessy, H. Maas, A. Devaux, U. Graf, *Solid State Sciences*, **2**, 421, (2000).
- [4] J. P. Langley, J. Hulliger *Chem. Soc. Revs.*, **28**, 279 (1999).
- [5] A. Douhal, T. Fiebig, M. Chachisvilis, A.H. Zewail, *J. Phys. Chem. A*, **102**, 1657 (1998).
- [6] Y. S. Park, S. Y. Um, K. B. Yoon, *J. Am. Chem. Soc.*, **121**, 3193 (1999).
- [7] D. W. Breck, *Zeolite Molecular Sieves*, John Wiley & Sons, New York, 1974.
- [8] W. M. Meier, D.H. Olson, C. Baerlocher, *Atlas of Zeolite Structure Types*, Elsevier, London, 1996.
- [9] S. L. Suib, *Chem. Rev.*, **93**, 803 (1993).
- [10] F. Schüth, *Chemie in unserer Zeit*, **29**, 42 (1995).
- [11] G. Calzaferri, M. Lanz, J. Li, *J. Chem. Soc., Chem. Commun.*, 1313 (1995).
- [12] K. B. Yoon, Y. S. Park, J. K. Kochi, *J. Am. Chem. Soc.*, **118**, 12710 (1996).
- [13] U. Vietze, O. Krauss, F. Laeri, G. Ihnlein, F. Schüth, B. Limburg, M. Abraham, *Phys. Rev. Lett.*, **81**, 4628 (1998).
- [14] S. D. Cox, T. E. Gier, G. D. Stucky, J. Bierlein, *J. Am. Chem. Soc.*, **110**, 2986 (1988).
- [15] L. Werner, J. Caro, G. Finger, J. Kornatowski, *Zeolites*, **12**, 658 (1992).

- [16] G. Schulz-Ekloff, In *Advanced Zeolite Science and Applications, Studies in Surface Science and Catalysis*, J. C. Jansen, M. Stöcker, H.G. Karge, J. Weitkamp, Eds., Elsevier; Amsterdam, 1994, Vol. 85, p. 145
- [17] M. Ehrl, F. W. Deeg, C. Bräuchle, O. Franke, A. Sobbi, G. Schulz-Ekloff, D. Wöhrle, *J. Phys. Chem.*, **98**, 47 (1994).
- [18] R. Hoppe, G. Schulz-Ekloff, D. Wöhrle, C. Kirschhock, H. Fuess, In *Zeolites and Related Microporous Materials: State of the Art 1994. Studies in Surface Science and Catalysis*, J. Weitkamp, H. G. Karge, H. Pfeifer, W. Hölderich, Eds., Elsevier, Amsterdam, 1994, Vol. 84, pp. 821-827.
- [19] J. Caro, F. Marlow, M. Wübbenhorst, *Adv. Mater.*, **6**, 413 (1994).
- [20] D. Wöhrle, G. Schulz-Ekloff, *Adv. Mater.*, **6**, 875 (1994).
- [21] V. Ramamurthy, D. R. Sanderson, D. F. Eaton, *J. Am. Chem. Soc.*, **115**, 10438 (1993).
- [22] M. Pauchard, A. Devaux, G. Calzaferri, *Chem. Eur. J.*, **6**, 3556 (2000).
- [23] D. Brühwiler, N. Gfeller, G. Calzaferri, *J. Phys. Chem. B*, **102**, 2923 (1998).
- [24] B. Müller, G. Calzaferri, *J. Chem. Soc., Faraday Trans.*, **92**, 1633 (1996).
- [25] B. Hennessy, S. Megelski, C. Marcolli, V. Shklover, C. Bärlocher, G. Calzaferri, *J. Phys. Chem. B*, **103**, 3340 (1999).
- [26] G. Calzaferri, N. Gfeller, *J. Phys. Chem.*, **96**, 3428 (1992).
- [27] F. Binder, G. Calzaferri, N. Gfeller, *Solar Energy Mat. and Sol. Cells*, **38**, 175 (1995)
- [28] F. Binder, G. Calzaferri, N. Gfeller, *N. Proc. Ind. Acad. Sci.*, **107**, 753 (1995).
- [29] M. Bockstette, D. Wöhrle, I. Braun, G. Schulz-Ekloff, *Microp. Mesop. Mater.*, **23**, 83 (1998).
- [30] P. Lainé, M. Lanz, G. Calzaferri, *Inorg. Chem.*, **35**, 3514 (1996).
- [31] D. Brühwiler, R. Seifert, G. Calzaferri, *J. Phys. Chem B*, **103**, 6397 (1999).
- [32] Z. G. Fetisova, A. M. Freiberg, K. E. Timpmann, *Nature*, **334**, 633 (1988).
- [33] X. Hu, K. Schulten, *Phys. Tod.*, **50**, 28 (1997).
- [34] W. Kühlbrandt, D. N. Wang, *Nature*, **350**, 130 (1991).
- [35] H. R. Kerp, H. Donker, R. B. M. Koehorst, T. J. Schaafsma, E. E. van Faassen, *Chem. Phys. Lett.*, **298**, 302 (1998).
- [36] V. Balzani, S. Campagna, G. Denti, A. Juris, S. Serroni, M. Venturi, *Sol. Ener. Mat. Sol. Cells*, **38**, 159 (1995).
- [37] V. Balzani, S. Campagna, G. Denti, A. Juris, S. Serroni, M. Venturi, *Coord. Chem. Rev.*, **132**, 1 (1994).
- [38] C. V. Kumar, A. Chaudhary, *Microp. Mesop. Mater.*, **32**, 75 (1999).
- [39] L. Jullien, J. Canceill, B. Valeur, E. Bardez, J.-M. Lehn, *Angew.Chem.*, **106**, 2582 (1994).
- [40] H. Bücher, K. H. Drexhage, M. Fleck, H. Kuhn, D. Möbius, F. P. Schäfer, J. Sondermann, W. Sperling, P. Tillmann, J. Wiegand, *Mol. Crystals* **2**, 199 (1967).
- [41] F. Willig, In *Photochemical Conversion and Storage of Solar Energy*, E. Pelizzetti, M. Schiavello, Eds., Kluwer Academic Publishers, Dordrecht, 1991, pp. 235-249.
- [42] N. Tamai, T. Yamazaki, I. Yamazaki, *J. Phys. Chem.*, **91**, 841 (1987).
- [43] J. A. Pescatore, Jr., I. Yamazaki, *J. Phys. Chem.*, **100**, 13333 (1996).
- [44] B. A. Gregg, U. Resch, *J. Photochem. Photobiol., A: Chem.*, **87**, 157 (1995).
- [45] S. E. Webber, *Chem. Rev.*, **90**, 1469 (1990).
- [46] D. M. Watkins, M. A. Fox, *J. Am. Chem. Soc.*, **118**, 4344 (1996).
- [47] V. Balzani, P. Ceroni, S. Gestermann, M. Gorka, C. Kauffman, M. Maestri, F. Vögtle, *ChemPhysChem*, **4**, 224 (2000).
- [48] D. M. Sturmer, D. W. Heseltine, In *The Theory of the Photographic Process*, T. H. James, Ed., Macmillan Publishing Co., New York, 1977, pp. 194-234.

- [49] C. A. Bignozzi, R. Argazzi, J. R. Schoonover, G. J. Meyer, F. Scandola, *Solar Energy Mater. Sol. Cells*, **38**, 187 (1995).
- [50] H. Tributsch, *Proc. IPS-10*, Z. W. Tian, Y. Cao, Eds., Intern. Academic Publishers, Beijing, 1993, pp. 235-247.
- [51] R. Memming, H. Tributsch, *J. Phys. Chem.*, **75**, 562 (1971).
- [52] N. Gfeller, S. Megelski, G. Calzaferri, *J. Phys. Chem. B*, **103**, 1250 (1999).
- [53] S. Megelski, G. Calzaferri, *Adv. Function. Mater.*, in press
- [54] S. Megelski, A. Lieb, M. Pauchard, A. Drechsler, S. Glaus, C. Debus, A. J. Meixner, G. Calzaferri, *J. Phys. Chem. B*, **105**, 23 (2001).
- [55] N. Gfeller, S. Megelski, G. Calzaferri, *J. Phys. Chem. B*, **102**, 2433 (1998).
- [56] M. Kasha, H. R. Rawls, M. Ashraf El-Bayoumi, *Pure Appl. Chem.*, **11**, 371 (1965).
- [57] E. G. McRae, M. Kasha, *J. Chem. Phys.*, **28**, 721 (1958).
- [58] M. Tsapatsis, T. Okubo, M. Lovallo, M. E. Davis, *Mat. Res. Soc. Symp. Proc.*, **371**, 21 (1995).
- [59] S. Ernst, J. Weitkamp, *Catal. Today*, **19**, 27 (1994).
- [60] P. A. Anderson, A. R. Armstrong, A. Porch, P. P. Edwards, L. J. Woodall, *J. Phys. Chem. B*, **101**, 9892 (1997).
- [61] G. Calzaferri, *Chimia*, **52**, 525 (1998).
- [62] T. Ohsuna, Y. Horikawa, K. Hiraga, *Chem. Mater.*, **10**, 688 (1998).
- [63] A. Kunzmann, R. Seifert, G. Calzaferri, *J. Phys. Chem. B*, **103**, 18 (1999).
- [64] S. Hashimoto, M. Hagiri, N. Matsubara, S. Tobita, *Langmuir*, in press.
- [65] J. S. Batchelder, A. H. Zewail, T. Cole, *Applied Optics*, **18**, 3090 (1979).
- [66] P. R. Hammond, *J. Chem. Phys.*, **70**, 3884 (1979).
- [67] G. Juzeliuñas, D. L. Andrews, In *Resonance Energy Transfer*, D. L. Andrews, A. A. Demidov, Eds., John Wiley & Sons, Chichester, 1999, pp. 65-107
- [68] T. Förster, *Ann. Phys (Leipzig)*, **2**, 55 (1948).
- [69] T. Förster, *Fluoreszenz organischer Verbindungen*, Vandenhoeck & Ruprecht, Göttingen, 1951.
- [70] D. L. Dexter, *J. Phys. Chem.*, **21**, 836 (1952).
- [71] K.B. Eisenthal, S. Siegel, *J. Chem. Phys.*, **41**, 652 (1964).
- [72] H. Kuhn, *J. Chem. Phys.*, **53** 101 (1970).
- [73] J. R. Lacowicz, *Principles Fluorescence Spectroscopy*, 2nd ed., Kluwer Academic/Plenum, New York, 1999.
- [74] T. Förster, In *Comparative Effects of Radiation*, Eds. M. Burton et al., Wiley New York, 1960, pp. 300-319.
- [75] N. Gfeller, G. Calzaferri, *J. Phys. Chem. B*, **101**, 1396 (1997).
- [76] G. Calzaferri, R. Rytz, *J. Phys. Chem.*, **99**, 12141 (1995).
- [77] M. Pfenniger, G. Calzaferri, *ChemPhysChem*, **1**, 211 (2000).
- [78] P. Lainé, R. Seifert, R. Giovanoli, G. Calzaferri, *New J. Chem.*, **21**, 453 (1997).
- [79] K. Ha, Y.-J. Lee, D.-Y. Jung, J. H. Lee, K. B. Yoon, *Adv. Mater.*, **12**, 1614 (2000).